Nano-structuring of a high entropy alloy by severe plastic deformation: experiments and crystal plasticity simulations

Surya N. Kumaran, Sudeep K Sahoo, Christian Haase, Luis A Barrales-Mora, Laszlo S Toth

Nano-structuring of a high entropy alloy by severe plastic deformation: experiments and crystal plasticity simulations

Surya N. Kumaran[a,b,*], Sudeep K. Sahoo[c], Christian Haase[d], Luis A. Barrales-Mora[b], Laszlo S. Toth[a,e,f,*]

[a]*Laboratoire dtude des Microstructures et de Mcanique des Matriaux (LEM3), Universit de Lorraine, Arts et Mtiers, 57070, Metz, France.*
[b]*Georgia Institute of Technology, CNRS IRL 2958, George W. Woodruff School of Mechanical Engineering, 57070, Metz, France.*
[c]*Universit de Bordeaux, I2M UMR CNRS 5295, Arts et Mtiers Institute of Technology, 33400, Talence, France.*
[d]*Steel Institute, RWTH Aachen University, 52072, Aachen, Germany.*
[e]*Laboratory of Excellence on Design of Alloy Metals for Low-Mass Structure (Labex-DAMAS), Universit de Lorraine, 57070, Metz, France.*
[f]*University of Miskolc, Institute of Physical Metallurgy, Metal Forming and Nanotechnology, 3515, Miskolc, Hungary.*

Abstract

The evolution of microstructure, texture, and mechanical properties of an induction melted non-equiatomic $Al_6Co_{23.5}Fe_{23.5}Mn_{23.5}Ni_{23.5}$ (at.%) high entropy alloy subjected to severe plastic deformation was investigated experimentally and by simulations. Analyses using electron backscatter diffraction and transmission Kikuchi diffraction images revealed the evolution of the microstructures. The coarse-grained initial structure was deformed down to an average grain size of 50 nm after a shear strain of 11 by employing the high-pressure compressive shearing process, at room temperature. Transmission electron microscopy analysis showed the presence of nano-twins. The high deformation led to a significant increase in the strength, up to $\approx$ 1.0 GPa. X-ray diffraction macro-texture analysis revealed a shear texture with the dominance of the $B/\overline{B}$ $\{112\}\langle 110\rangle$-type component whose intensity varied with strain. A two-step Taylor-type polycrystal plasticity simulation approach reproduced the texture by a correlation value of 91%. In the first part of the modeling, grain fragmentation was simulated, while in the second part, grain boundary shearing and deformation twinning were considered together with the operation of $\{111\}\langle 112\rangle$-type partial slip. The effect of twinning was also examined in the texture modeling and the simulations esti-

*Corresponding authors
Email addresses: surya-nilamegam.kumaran@univ-lorraine.fr (Surya N. Kumaran), laszlo.toth@univ-lorraine.fr (Laszlo S. Toth)

mated that its fraction was less than 2%.

Keywords: High-entropy alloys, Severe plastic deformation, Crystallographic texture, Polycrystal plasticity, High-pressure compressive shearing.

1. Introduction

High entropy alloys (HEAs) or multi-principal element alloys (MPEAs) or complex concentrated alloys (CCAs) are a novel class of metallic materials that consist of four or more elements in equal or near-equal atomic percent (> 5 at.% for each component) with a possible addition of minor elements as well (< 5 at.%) [1]. HEAs may show unique and attractive engineering properties [2–4] when compared to conventional alloys. Even though these alloys are widely referred to as "HEAs", MPEAs and CCAs are also used by a number of researchers owing to the challenges to the entropy-based definition of HEAs [5]. In the present contribution, the processed alloy is referred to as HEA, because a single-phase solid solution was pursued and indeed obtained.

Great efforts are being invested in exploring the compositional space available in HEAs [6, 7]. Unexpected properties are seen as a consequence when the solid solution phase stability is influenced by controlling the configurational entropy. Extensive research on these alloys shows that; they form simple solid solutions (body-centered cubic (bcc) or face-centered cubic (fcc) or hexagonal close-packed (hcp) or mixed), even though several elements are combined to form a HEA [1–5, 8]. It is seen that substitutional elements have a major impact on the mechanical properties of HEAs. The interaction of Al and Cr is found to be repulsive and weakest when the mixing enthalpy (ΔH_{mix}) values of several binary systems made with elements such as Al, Co, Cr, Cu, Fe, Mn, Ni, and Ti are compared [9]. The addition of Al is aimed to increase the strength of the alloy [4, 8, 10]. The strength of a HEA is increasing with an increase in Al content, but its ductility declines [4, 11]. Fcc HEAs demonstrate comparable mechanical properties to conventional alloys like austenitic stainless steels or Ni-based alloys [8].

The adjustment of stacking fault energy (SFE) is an important parameter in structural applications as it governs physical mechanisms such as slip system activity, twinning-induced plasticity (TWIP) or transformation induced plasticity (TRIP) [12, 13]. Due to the possibility of numerous combinations in HEAs, a tool combining CALPHAD and additive manufacturing is developed by

Kies et al. [14] to screen the alloys. First the CALPHAD technique is used to determine the composition of the alloys of interest; then additive manufacturing is utilized to study the alloys. This tool also determines that the elimination of Cr from the Cantor alloy prevents carbide formation and increases the SFE. Further, addition of Al influences phase stability and SFE but also decreases the overall density of the HEA [12]. The study on effect of interstitial atoms in HEAs are yet to be well explored. The influence of Al and C on the SFE in a CoFeMnNi alloy is studied by both experiments and by density function theory (DFT)-based modeling [14]. The Al_6CoFeMnNi HEA evinced in the calculations the lowest SFE, which would result in a higher propensity to twinning and thus the highest work hardening capacity of the studied alloys. For these reasons, this alloy has promising properties that can be explored and was, thus, chosen. It is predicted that the maximum solubility of Al in the CoFeMnNi- fcc matrix is around 6 at.%. Beyond that, Al forms a disordered B2 phase along with the fcc phase. Tensile testing results on Al_6CoFeMnNi HEA produced by the laser powder bed fusion technique indicate that the ultimate tensile strength is 0.62 GPa with a uniform elongation of 26.2%. The presence of a disordered B2 phase is confirmed by Karati et al. [15] in the homogenized equiatomic AlCoFeMnNi HEA.

Grain refinement is one of the successful ways to improve material properties, like strength and ductility. Due to the severe lattice distortion in HEAs, dislocation motion is more difficult compared to conventional alloys [16]. The grain refinement tendency of Cantor alloy has shown a higher Hall-Petch slope than conventional fcc metals. This has been associated to a possibly higher slip transfer resistance at grain boundaries in HEAs [8]. Liu et al. [16] found that the grain growth and strength of Cantor alloy exhibits classical Hall-Petch relationship, however, the hardening coefficient was found to be significantly larger than for coventional fcc metals and alloys. Similar observations have been made by Gwalani et al. [17] in $Al_{0.3}$CoCrFeNi HEA. Huang et al. [18] also found the same result by comparing FCC HEAs, medium entropy alloys (MEAs), and conventional alloys. Their experiments proved that the hardness and grain size of these HE/ME alloys follow the classical Hall-Petch relation. In their investigation, it was also also found that the Hall-Petch coefficient is mostly affected by the materials SFE and shear modulus, with an exception for CoCrFeMnNi.

Microstructure and texture investigations at lower strains have been carried out extensively [8, 19]. A detailed insight into the microstructure and texture evolution of HEAs subjected to high

plastic strains are rare and a better understanding of the underlying mechanisms is required. Strain hardening of a HEA is rarely measured during large deformation, while it is a common way to strengthen polycrystalline materials [20–22]. This can be achieved conventionally by rolling and subsequent annealing [23–25] but also by severe plastic deformation (SPD) techniques [26, 27]. It is seen in many SPD techniques that it leads to extensive grain refinement in metals [22]. The most widely applied SPD techniques to achieve large shear deformations are equal channel angular pressing (ECAP) [28] and high-pressure torsion (HPT) [29]. Some HEA compositions have been studied after undergoing SPD, especially by HPT [20, 26, 30]. For instance, Shahmir et al. [30] successfully deformed CoCrFeMnNi HEA by ECAP achieving an ultimate tensile strength of ≈ 0.99 GPa and a maximum hardness of ≈ 315 HV after multiple passes.

In the current contribution, high-pressure compressive shearing (HPCS) SPD technique was employed to deform Al_6(CoFeMnNi) HEA and refine its grain structure. HPCS results in a high shear strain in just one pass with a homogenous microstructure. The key advantage of using HPCS in comparison to any other SPD technique is that it can provide strain hardening curves [31]. HPCS is comparable with the high pressure sliding (HPS) process [32] as both can produce strains in similar ranges. The maximum strain produced by HPCS till to date is ε_{eq}= 33.3 (grain size = 181 nm) on ARMCO steel [31]. In turn, HPS has demonstrated that a maximum of ε_{eq}= 24.6 can be achieved after a sliding distance of 30 mm [32]. Lee et al. [33] processed AA7075 alloy by HPS under a pressure of 1.0 GPa for sliding distances of 7.0 mm (ε_{eq}= 5.8) and 10.0 mm (ε_{eq}= 8.2). This alloy underwent considerable grain refinement up to ≈ 280 nm at room temperature. Nevertheless, both HPCS and HPS are new techniques with up-scalable possibilities. Likewise, Schuh et al. [26] explored the CoCrFeMnNi HEA after subjecting it to SPD and obtained an exceptional grain refinement of ≈ 50 nm, strength of ≈ 1.95 GPa and a hardness of ≈ 520 HV, albeit, with low ductility, which is inherent in low temperature SPD processes. Gubicza et al. [34] compared CoCrFeMnNi and CoCrFeNi subjected to SPD. After HPT, the grain size of the CoCrFeNi HEA saturates at 80 nm, while the hardness is ≈ 520 HV. The grain refinement in this case is correlated to the involvement of deformation twinning with rapid increase and multiplication of dislocations during HPT. Similar observations have been made during HPT of CoCrFeMnNi [35] with a grain size reduction up to 27 nm.

X-ray diffraction (XRD) techniques are utilized to study the microstructure at high strains, and

synchrotron diffractions for phase transformations [36]. However, because of the extremely low grain size after SPD of HEAs, grain morphologies and intragranular features require advanced methods, like transmission Kikuchi diffraction (TKD). Although the deformation texture evolution during various deformation processes of fcc HEAs has been studied [19], to our knowledge, only few investigations [36, 37] have been conducted to unravel the evolution of the textures and microstructures of large strain-deformed HEAs.

A crystal plasticity framework allows by material physics-based principles to simulate the texture development during deformation while simultaneously offering insight into the underlying deformation mechanisms. Sonkusare et al. [37] applied viscoplastic self-consistent (VPSC) crystal plasticity simulation with partial planar slip and octahedral slip to obtain the characteristic shear texture of a severely deformed CoCuFeMnNi HEA. However, to the authors knowledge, there are no more studies reported in the literature on polycrystal simulations of highly deformed HEAs. In the present work, multiple deformation mechanisms incorporated in Taylor-type polycrystal model were utilized to successfully simulate the texture evolution at high plastic strain.

In this work, Al_6(CoFeMnNi) HEA was deformed by SPD using the HPCS technique up to a shear strain of 11. The microstructure and texture evolution along with its resulting mechanical properties at intermediate levels of strain were studied employing advanced characterization techniques and modeling approaches to address the following fundamental scientific questions; (i) What are the active deformation mechanisms involved during SPD of the investigated HEA? (ii) How do these mechanisms govern the microstructure and texture evolution in fcc HEAs at very high plastic strain? (iii) How can the deformation behavior and related texture evolution be modeled using polycrystal plasticity?

2. Methods

2.1. Experimental methods

Material

A non-equiatomic Al_6(CoFeMnNi) HEA was induction melted in a cold crucible using pure metals (at least 99.8% purity) in argon atmosphere and crystallized as a single phase fcc alloy. The chemical composition of the alloy is listed in Table 1. The as-cast cylinder was homogenized by

annealing at 1423 K for 2 h under an argon atmosphere with furnace cooling. A rectangular bar with 80 mm (length) x 20 mm (width) x 20 mm (thickness) was re-melted from the cylinder. The rectangular bar (hereafter referred to as the initial sample) was again homogenized by annealing at 1423 K for 2 h under vacuum. Thin rectangular sheets (dimensions are listed in Table 2) were cut from the rectangular bar to be severely deformed at ambient temperature.

Processing by high-pressure compressive shearing (HPCS)

After the homogenization treatment, the rectangular sheet specimen was deformed by HPCS. This process is a new variant of the high-pressure shearing (HPS) process [32]. This technique was designed to overcome the sample limitation in the HPT process and to achieve high shear strains in a single pass. HPCS uses rectangular thin sheets to replace the circular discs of HPT. The mechanics behind the HPCS process is described in detail by Toth et al. [31]. This SPD technique has demonstrated enhanced grain refinement and mechanical properties under simultaneous high compression pressure and shear. The experiments for the current contribution were carried out on the same installation as in Ref. [31]. Three punches were used, depicted as P1, P2, and P3 in Fig. 1a. A plunger was placed between the three punches to accommodate two samples. In HPCS, the samples are subjected to a compressive force F_N and a shear force F_s. The compressive force was provided by punch P1, while the punch P3 produced the necessary shear force. The stability of the process was improved by the back-pressure punch, P2. To eliminate the friction of the plunger with the die, two identical samples, called top and bottom samples, were placed on the plunger, as shown in Fig. 1. A schematic of the HPCS deformation process is shown in Fig. 2. The dimensions of the samples, i.e., the initial thickness and length are denoted as t_0 and l_0 respectively. The width of the samples remained constant throughout the process, constrained by the die. The plunger was moved by a displacement s. There was no slipping of the samples between the plunger and the punch P1, due to a sufficiently large compressive force between them, and also by good preparation of the plunger surface by previous sand blasting. The experiments were carried out at ambient temperatures up to different strain values.

The compression (ε) and shear (γ) strains, as well as the equivalent strain (ε_{eq}) in one testing

can be calculated using the formulas [31]:

$$\varepsilon = \int_0^{\varepsilon} d\varepsilon = \int_{t_0}^{t_F} \frac{dt}{t} = ln\frac{t}{t_0}, \gamma = \int_0^{\gamma} d\gamma = \frac{1}{2.t_0.l_0}\left((l_0 + s)^2 - l_0^2\right), \quad (1a,b)$$

$$\varepsilon_{eq} = \frac{1}{\sqrt{3}a}(b - c) + \frac{1}{2\sqrt{3}}\left[ln\left|\frac{a-b}{a+b}\right| - ln\left|\frac{a-c}{a+c}\right|\right], \quad (2)$$

Where the notations $a = 2.t_0.l_0$, $b = \sqrt{a^2 + (s + l_0)^4}$, and $c = \sqrt{a^2 + l_0^4}$ are used. The equivalent stress is calculated from:

$$\sigma_{eq} = \tau\sqrt{3 + 48\left(\frac{\dot{\varepsilon}}{\dot{\gamma}}\right)^2}. \quad (3)$$

where $\dot{\varepsilon}$ and $\dot{\gamma}$ are the compressive and shear strain rates, respectively. The parameters and the calculated strain values of the HPCS tests are given in Table 2.

Characterization

The phase characterization of the initial sample was conducted using XRD with Co-Kα (λ= 1.79 Å) radiation in a Brucker D8 advanced diffractometer. As displayed in Fig. 3a, the single fcc phase of the initial sample has three major peaks with a lattice parameter of a = 3.60 Å. The flat middle part of the deformed sample was considered for characterization in all samples. Electron back-scattered diffraction (EBSD) and TKD techniques [38] were utilized for the microstructural characterization. JEOL 6490 and JEOL F-100 scanning electron microscopes (SEM) equipped with Oxford EBSD detectors were utilized to perform the microstructural analysis. The samples for EBSD analysis were prepared by cutting the deformed sample at the mid-width portion on the x-y plane (Fig. 2). The sectioned samples were initially polished with SiC grit papers up to P4000 followed by 3 μm diamond polishing. Finally, electro-polishing in an electrolyte containing 700 ml ethanol (C_2H_5OH), 100 ml butyl alcohol ($C_6H_{14}O_2$), and 78 ml perchloric acid ($HClO_4$) at 19 - 22 V for 18 s was performed. To perform TKD, transmission electron microscopy (TEM), and forward scattered diffraction (FSD), thin (150-200 nm thickness) foils were extracted (using the guidelines found in [39]) from the samples using the focused ion beam (FIB) milling technique in a Zeiss Auriga SEM. Further, nano-level characterization was carried out using the bright-field and dark-field images obtained from a Philips CM 200 keV TEM.

Macro-textures of the deformed alloys were determined using a Siemens D5000 X-ray diffractometer. The samples for XRD were analyzed on the surface defined by the x-y plane, as shown in Fig. 2. The processing and analysis of the microstructure and texture files were performed using the ATEX software [40].

Hardness

Nanoindentation tests were performed using the NHT^2 nano-indenter manufactured by Anton Paar and equipped with a Berkovich tip (142.3°). The indents were carried out with a load of 10 mN for a holding time of 5 s. Vickers microhardness tests were also performed using a Zwick Roell Vickers hardness tester (ZHV) at 500 g, for a dwell time of 10 s. The distances between the indents were at least 2.5 times the diagonal value of the indents.

2.2. Modeling approaches

In this work, the evolution of the texture was modeled by a Taylor-type polycrystal model, considering grain fragmentation, grain boundary shearing, and deformation twinning along with self and latent hardening of the slip systems. The integration of the above-mentioned deformation mechanisms into the Taylor-type polycrystal approach are discussed below.

Grain fragmentation based on lattice curvature

Based on the lattice curvature developing within the grains of a polycrystal during plastic deformation, a grain fragmentation approach was developed by Toth et al. [41]. In that modeling, the grain interior is divided into two zones: (i) zone near the grain boundary and (ii) zone unaffected by the grain boundary (central zone). Before deformation, the lattice planes are considered to be perfectly planar. During deformation, these planes are rotating from their original state. The rotations of these crystallographic planes are considered to be different in the two zones; slower near the grain boundary which gives rise to lattice curvature. In the grain boundary-zone, the lattice spin ($\underline{\dot{\Omega}}_{SG}$) is lower by a factor of $(1-\mu)$:

$$\underline{\dot{\Omega}}_{SG} = (1-\mu)\,\underline{\dot{\Omega}}_{G}. \tag{4}$$

The parameter μ is a lattice curvature coefficient and its value ranges from 0 to 1. The misorientation between the central region and the external regions of the grain is calculated at each incremental strain during the computation. When the misorientation reaches a minimum value (5°), that fragment is considered as a new grain and sub-divided into 3x3x3 parts, like the original parent grain. The fragmentation of a 3D parent grain into sub-grains can be viewed as a Rubik cube. These fragmented grains will further deform like the parent grain and the process is repeated within the new embedded Rubik structure. The computer code permitted to have three embedded levels, which potentially could refine a grain into 27x27x27= 19683 small grains. Because of the huge increase in the grain number due the grain fragmentation process, initially only 500 grains were selected to represent the (random) distribution of grain orientations.

It is important to note that although Taylor (uniform) deformation mode was imposed on the grains, by imposing a different lattice spin in the GB region, the deformation of a slowed-down grain is actually different from the macroscopic one. Indeed, while the plastic strain gradient was imposed to be the same ($\underline{\underline{F}}^p$), the difference in the rotation ($\underline{\underline{F}}^*$) involves a modified deformation gradient, as can be seen from the polar decomposition of the total deformation gradient: $\underline{\underline{F}} = \underline{\underline{F}}^*.\underline{\underline{F}}^p$. Therefore, the used grain fragmentation approach was not a fully Taylor polycrystal plasticity model. Nevertheless, one can refer to it as a Taylor-type model.

Implementation of the hardening law

The simulation of the strain hardening for any deformation process is another crucial factor that needs to be considered. Within the framework of crystal plasticity, the evolution of flow stress during plastic strain is frequently modeled using the self and latent hardening of the slip systems. The approach employed in the present work is introduced by Kalidindi et al. [42] and further modified by Zhou et al. [43]. It expresses the influence of all the slip systems on the hardening rate of a given slip system by:

$$\dot{\tau}_0^i = \sum_{j=1}^{n} q^{ij} h \left(1 - \frac{\tau_0^i}{\tau_{sat}^i}\right)^a . \left|\dot{\gamma}^j\right| . \tag{5}$$

Here τ_0^i is the shear resistance of the slip system i, $\dot{\gamma}^j$ is the resolved shear strain rate. The total number of slip systems is represented by n and q^{ij} denotes a (n x n) matrix and accounts for the self and latent interactions between the slip systems. The diagonal elements of q^{ij} represent

the effect of self-hardening, while the off-diagonal parts are the latent hardening terms [44]. The strain hardening parameters are h, a, and τ^i_{sat}. Recently, Sahoo et al. [45, 46] proposed a simplified expression of Eq. 5 to be used at the macroscopic scale. Using this simplified function and the Taylor factor it is possible to obtain reasonable values for the h, a, and τ^i_{sat} parameters, and can be fine-tuned by a small number of iterations.

Incorporation of grain boundary shearing in polycrystal modeling

Zhao et al. [47] established a theoretical frame to model the effects of grain boundary sliding on the texture evolution of nano-crystalline materials. Here, we adopted the same modeling approach, however, changed the name of the deformation process from grain boundary sliding to grain boundary shearing (D. Molodov, Personal Communication, July 19, 2022). The reason for this is that a sliding process can be only imagined with flat grain boundaries, which is rarely the case in the microstructure. Another difficulty with sliding is the presence of triple junctions, which can stop the sliding. Indeed, a shear deformation process parallel to the boundaries even curved can be readily accommodated by the microstructure, and this is what was built into the grain boundary sliding model of Zhao et al. [47].

In the adopted modeling approach [47], the grains are considered as regular dodecahedrons, so the grain boundaries are flat. For the slip behavior within the grain interior, the general power law is used, which relates the slip rate ($\dot{\gamma}$) and resolved shear stress (τ) by the viscoplastic constitutive relation [48–52]:

$$\dot{\gamma}^{(s)} = \dot{\gamma}_0^{(s)} \left(\frac{\tau^{(s)}}{\tau_0^{(s)}} \right) \left| \frac{\tau^{(s)}}{\tau_0^{(s)}} \right|^{1/m-1} . \tag{6}$$

Here $\dot{\gamma}^{(s)}$ is the slip rate in the slip system indexed by (s), $\dot{\gamma}_0^{(s)}$ is the reference slip rate corresponding to the reference resolved shear stress $\tau^{(s)}$, and $\tau_0^{(s)}$ is the operating resolved shear stress. m is the viscosity coefficient which is considered independent of the strain rate [47, 53]. Similarly, the same constitutive equation is also applied for the shearing of the grain boundaries, however, assuming linear viscous behavior:

$$\dot{\gamma}^{(GB)} = \dot{\gamma}_0^{(GB)} \left(\frac{\sigma_{ij}^{Mac} m_{ij}^{GB}}{\tau_0^{GB}} \right). \tag{7}$$

Here $\dot{\gamma}^{(GB)}$ and τ_0^{GB} signifies the grain boundary shearing rate and the resolved shear stress on the grain boundary, respectively. The grain boundary undergoes shearing by shear stress parallel to its plane. The shearing direction of the grain boundary is the direction of the maximum shear stress obtained from the macroscopic stress state. The magnitude of the shear stress is obtained by the projection of the macroscopic stress tensor on the grain boundary shearing system (defined by m_{ij}^{GB}):

$$\tau^{(GB)} = \sigma_{ij}^{Mac} m_{ij}^{GB}. \tag{8}$$

Twinning approach

As nano-twins were detected in the microstructure, twinning was incorporated into the grain boundary shearing-Taylor polycrystal code. The "All Twin Variant (ATV)" approach [54], originally developed for hcp-structured materials, was adapted to the fcc case. The principle of ATV modeling is that all twin variants are considered and allowed to grow progressively during deformation. 'Twin-grains' are created before deformation pertaining to the twinning orientations for each of the parent grains, initially with zero-volume fraction [54–56]. This ATV scheme proved to be very efficient for hcp materials, where multiple twin variants can be active at the same time [54, 57]. However, for fcc metals, since only one variant is dominating, the ATV scheme was modified to consider only the most active twin variant. With this modification, the ATV scheme resembles to the PTR (Predominant Twin Reorientation) scheme established by Tomé et al. [58]. The major difference is that in this simplified ATV approach, the twin variant coexists with the mother grain, while in the PTR modeling, the mother grain is fully replaced by the twin when it reaches a critical value. Therefore, in the present modified ATV approach, owing to significant lattice rotation during large strain deformation, a different twin variant can become the most active one, so replacing the previous dominant variant, which would then cease to grow. This situation actually did take place in our polycrystal simulation, so the average number of twin variants went up to about two per grain at a strain of 6.5.

For fcc crystals, the $\{111\}\langle 112\rangle$ partial slip systems represent the twin variants [56]. The activity of the $\{111\}\langle 112\rangle$ slip systems was calculated within the parent grains using the same constitutive law as for normal crystallographic slip (Eq. 6). The increase in the volume growth of

a twin variant (ΔV_s) was modeled by assigning them a part of the volume of their respective parent grain:

$$\Delta V_s = V_{parent} \frac{\left|\dot{\gamma}^s_{twin}\right| .\Delta t}{\gamma_{twin}}, \tag{9}$$

Here, V_{parent} is the actual volume of the parent grain and γ_{twin} is the crystallographic shear strain for twin creation ($1/\sqrt{2}$). The ratio $\left(\left|\dot{\gamma}^s_{twin}\right| .\Delta t\right)/\gamma_{twin}$ is the fraction of the shear deformation in the twin system with respect to the twin-shear. ~~The ATV approach was shown to be very effective in several modeling studies~~.

Two-step modeling approach

As it was presented in the previous sections, additional to crystallographic slip, three other deformation mechanisms that can be relevant in modeling of large strain behavior of HEAs must be considered, namely, grain fragmentation, grain boundary shearing, and deformation twinning. The relevance of these mechanisms depends on the state of the plastic deformation. Grain fragmentation starts quite soon at the beginning of plastic strain with a high rate, then slows down, finally arrives into a steady state, where the average grain size is constant. Grain boundary shearing, on the other hand, is not operational before the grain size becomes sufficiently small. Deformation twins were active throughout the severe deformation, they were seen in the form of nanotwins. As it is rather complicated to combine the three mechanisms into a single polycrystal code, a sequential modeling approach was set up; (i) first grain fragmentation based on lattice curvature and (ii) grain boundary shearing using the Taylor-type polycrystal model with twinning. The grain fragmentation simulation was used until the steady state was reasonably reached; at an equivalent strain value of 4.0, as was evidenced from the experiments. From this deformation stage, the remaining strain part was simulated using grain boundary shearing-Taylor polycrystal model with deformation twinning. The output texture from the grain fragmentation simulation was served as an input for the grain boundary shearing-Taylor polycrystal simulation.

Velocity gradient for HPCS

The key input to any polycrystal modeling is the velocity gradient tensor which describes the deformation process of a material element similar to that of the experimental scenario. In HPCS,

the velocity gradient tensor ($\underline{\underline{L}}$) has three non-zero components, with $\dot{\varepsilon}$ the thickness strain rate and $\dot{\gamma}$ is the shear strain rate [31]:

$$\underline{\underline{L}} = \begin{pmatrix} \dot{\varepsilon} & -\dot{\gamma} & 0 \\ 0 & -\dot{\varepsilon} & 0 \\ 0 & 0 & 0 \end{pmatrix}. \tag{10}$$

The analytical expressions of the two strain rate parameters are [31]:

$$\dot{\varepsilon} = \frac{\dot{s}}{l_0 + s}, \dot{\gamma} = \dot{s}.\frac{(l_0 + s)}{h_0.l_0}. \tag{11a,b}$$

The large strain simulations were carried out incrementally, using small strain increments (0.01).

3. Results

3.1. Experimental results

Microstructure evolution

The initial state of the material was a single-phase fcc alloy with a coarse grain microstructure and an average grain size of 170 μm, as displayed in Fig. 3b. The samples were subjected to the HPCS deformation process up to three different von-Mises equivalent strain values; 1.8, 4.8, and 6.5. The obtained microstructures are displayed in Figs. 4-6. A tolerance angle of 5° was imposed to detect the grains in all EBSD and TKD images. High angle grain boundaries (HAGBs) (>15°) are represented by black lines and special $\Sigma3(111) - 60°$ twin boundaries (up to 8.66° deviation) are represented by white lines. In all IPF maps (Figs. 4-6) there are gray spots corresponding to unindexed regions as noise reduction was not performed. Neighbor-to-neighbor misorientation distribution graphs were also calculated and are exhibited along with the IPF maps. A minimum misorientation angle of 5° was employed to obtain the distributions, and the bin size was 1° in the figures. The solid black line in each graph represents the random distribution.

Due to the severe deformation process, the initial coarse grain microstructure transformed into an ultrafine-grained structure. After a deformation of ε_{eq}= 1.8, the average grain size was 32 μm and shear bands appeared, as shown in Fig. 4a. A high peak can be seen close to 20° misorientation

angle, as displayed in Fig. 4b. This can be correlated to the initiation of grain fragmentation. High orientation gradients can be seen in the microstructure (indicated by the varying colors within grains), which is the reason for the relatively low indexing rate ($\approx$ 76%) compared to the case for the initial sample ($\approx$ 99%).

The microstructures of the highly strained ($\varepsilon_{eq} > 1.8$) samples could not be studied using conventional EBSD technique due to the relatively low resolution of EBSD. Indeed, the grain size became so low at higher strains, that they could not be resolved by EBSD. Keller et al. [59] introduced transmission electron-based acquisition instead of back-scattered electrons i.e. TKD. This technique was used in the present work to study the microstructure at higher strains (ε_{eq}= 4.8 and 6.5). The obtained TKD-IPF maps of the samples, deformed up to ε_{eq}= 4.8 and 6.5, are shown in Fig. 5a and 6a, respectively. At these high strains, the grain fragmentation process led to the formation of nano-sized grains. The grain size decreased to an average value of $\approx$ 65 nm at ε_{eq}= 4.8 and to $\approx$ 50 nm at ε_{eq}= 6.5.

In the current study, the fact that orientation determination using TKD in the interior of the grains was successful but not near grain boundaries seems to substantiate the existence of a highly deformed zone near the grain boundaries and thus, the occurrence of grain boundary shearing. In fact, measurements of the misorientation across grain boundaries showed a strong orientation gradient as the line scan approached the grain boundary. Some features of the very highly deformed state shown in Fig. 6d can be considered as indications of the occurrence of grain boundary shearing: these are the gray, unindexed orientation zones around almost all grains. While the grain boundaries were clearly resolved as thin lines at lower strain (ε_{eq}= 4.8, Fig. 5a), the TKD technique could not resolve the orientations near the grain boundaries at the strain of 6.5 at similar grain size. This result seems to indicate that grain boundary shearing operates during large strain deformation of the alloy since this phenomenon is known to cause high localized orientation gradients at grain boundaries that would make an orientation determination extremely challenging and nearly impossible at large strains near grain boundary regions. Similar observations have been made, for instance, in a previous study in a BCC refractory HEA [60], where grain boundary shearing was clearly proven. In this investigation, specimens were marked with a regular quadratic grid and then deformed at elevated temperatures. After deformation, the grid was distorted in the direction tangential to the grain boundaries, which clearly evinced grain boundary shearing. Furthermore, near

the grain boundaries the specimens showed a strong localized deformation, which was substantiated by electron microscopy and by the onset of recrystallization along the grain boundaries in the form of a necklace structure. Furthermore, in ceramics materials, where grain boundary shearing is a more prominent deformation mechanism, it has been observed this phenomenon to cause the amorphization of grain boundary regions [61]. Evidently, in this case also an orientation determination would not be possible. In general, direct evidence of grain boundary shearing is difficult in case of severely deformed alloys due to the presence of high dislocation densities. Nevertheless, it is stressed that besides the arguments discussed here, simulation results also substantiated grain boundary shearing as a mechanism for texture development as discussed in Section 4.2.

FSD and TEM imaging techniques were used to confirm the presence of deformation induced nano-twins. The FSD images (Figs. 5b and 6b) reveal the presence of elongated nano-twins at specific spots (black rectangles in the figures). To further verify the twins, TEM bright-field images, dark-field images and their corresponding selected area diffraction patterns (SAED) (Fig. 7) were taken at ε_{eq}= 4.8 and ε_{eq}= 6.5. These observations confirmed the twin orientation relationships between the twins and the matrix, as shown in Figs. 7a and 7c. The twins were seen in bundles which were highly distorted due to the high deformation. The thickness of these deformation induced nano-twins ranged from 6 to 10 nm. The SAED with $[011]_{fcc}$ diffraction zone axis (Fig. 7b) was also employed to corroborate the presence of nano-twins. The TEM images Fig. 7k and 7l shows the overall microstructure at ε_{eq}= 4.8 and ε_{eq}= 6.5 respectively. The microstructure at ε_{eq}= 6.5 showed heavily deformed grains and evidence of high dislocation density.

Texture evolution

The crystallographic textures were determined by XRD, and then analyzed by the ATEX software [40]. They are presented here in terms of {111} pole figures and also by orientation distribution functions (ODFs), in two φ_2= const. sections of Euler space: at φ_2= 0° and 45°, as shown in Fig. 8. These two sections contain the main ideal components of fcc shear textures; they are listed in Table 3 [62]. These components are situated along two fibers: the A and B, which are defined by {111}|| shear plane normal, and ⟨110⟩ || shear direction, respectively. The A_1^*, $\bar{A}$, A_2^*, and A are on the A fiber, while the C, B, A, $\bar{A}$, and $\bar{B}$ are on the B fiber.

As can be seen in Fig. 8, the texture was a characteristic shear texture, well developed already

at the lowest strain. Though all the shear texture components were present, there were significant changes took place at higher strains: the $B/\overline{B}$ $\{112\}\langle 110\rangle$ and $A/\overline{A}$ $\{111\}\langle 110\rangle$ components strengthened, while the C and A_1^*/A_2^* components decreased in intensity. The volume fractions of the main ideal components were calculated using a maximum misorientation angle of 10° around the ideal position and displayed in Fig. 9a. It can be seen that the $B/\overline{B}$ is the major component, however, its intensity decreases at the highest strain. Indeed, the general ODF intensity of the texture first increased, then decreased. The strength of the texture can be represented by the so-called texture index, which is defined by the integral of the square of the ODF intensity over the whole orientation space [63]. The texture indices are displayed in Fig. 9b and reveal relatively low values at all stages of deformation.

Mechanical properties

During the HPCS process, it is possible to determine the strain hardening curves [31]. The equations that can be used for this purpose were presented in Eqs. 2 and 3, and the obtained results are displayed in Fig. 10. As can be seen, the results of the three tests curves are reasonably overlapping. The strain hardening curves clearly stabilized around 1.07 GPa. The strain hardening rate was very high up to about the equivalent strain of 1.0, then stabilized at a very low rate, showed by the blue continuous line in Fig. 10. In this approximately linear stage, the strain hardening rate was 8.6 MPa.

The nanoindentation (H_{IT}) and the microhardness values as a function of strain are shown in Fig. 10. The H_{IT} was extracted from the unloading part of load-depth curves using the Oliver and Pharr model [64]. The average difference between the average hardness value and the maximum and minimum values were utilized to represent the error bars. From the nanoindentation and microhardness tests, it is inferred that as the strain increased, the hardness of the material increased steadily. A maximum value of 4.2 GPa was obtained for microhardness at ε_{eq}= 6.5.

3.2. Simulation results

Comprehensive modeling work was carried out to simulate the texture evolution during HPCS. Taylor-type polycrystal plasticity simulation approach was used with several deformation mechanisms. The key mechanisms that can impact the texture evolution are: (i) the polycrystal model,

(ii) the deformation mode given by the velocity gradient, (iii) the slip systems with their respective strengths, and (iv) the input texture. A Taylor-type polycrystal model was considered along with a variable velocity gradient (as discussed in Section 2.2). An initially random texture was used for the simulations. The proposed operating slip systems in nano-sized fcc metals and alloys are the $\{111\}\langle 110\rangle$ and $\{111\}\langle 112\rangle$ [65, 66], which were also used in the present work with a reference strength ratio of $\tau_0^{<110>}/\tau_0^{<112>}$= 1.25. The viscosity parameter (m in Eq. 6) was 0.166 in all simulations. The parameters for the hardening were: h= 750 MPa, a= 2.4, and τ_{sat}= 728 MPa. These values were obtained by a small number of iterations using the technique of Sahoo et al. [45]. The simulated and experimental strain hardening curves are shown in Fig. 10 for comparison. It can be seen that the simulation was able to reproduce the strain hardening curve up to an equivalent strain of 2.

The simulated and experimental textures were compared using the scalar direct correlation parameter available in the ATEX software [40]. It is defined by the following calculation:

$$D = \frac{\int_g f_A(g) f_B(g) dg^2}{\sqrt{\int_g f_A^2(g) dg^2 . \int_g f_B^2(g) dg^2}}. \tag{12}$$

Here $f_A(g)$ and $f_B(g)$ are the ODFs of the two textures to be compared, with g being the orientation vector defined by the three Euler angles. The value of D can be between 0 and 1. A better correlation corresponds to a higher D value; for D= 1 the two textures are identical. In the present work, D is presented in percentages; so, 100% would be D= 1.

Texture obtained by two-step modeling

The best agreement between the experimental and simulated textures was obtained when the initial grain fragmentation simulation was followed by the grain boundary shearing simulation. This change in simulation was done at about ε_{eq}= 4 where, the strain hardening curve seemed to be stabilized and the grain size was in nano-scale (experimentally).

As the initial sample had a coarse grain microstructure with random orientations, a set of 500 randomly selected grain orientations was utilized as the input orientation distribution. Due to the grain fragmentation process, this initial grain number increased up to 6176765 grains after a strain of ε_{eq}= 4. The rate of grain fragmentation was controlled by the lattice curvature coefficient (μ) for which the value of 0.5 was found to be optimum. This value agrees with that of previous

simulations [67] and led to an average grain size of $\approx 30\ \mu$m. For the detection of new grains, the minimum misorientation angle of 5° was adopted in the simulation.

This first simulation work was continued then by another one, where grain fragmentation was stopped and grain boundary shearing was considered. For this purpose, the output texture obtained from grain fragmentation was used. A very large number of grain orientations were used to represent this texture: 50000-grain orientations were discretized with the help of the ATEX software [40]. Indeed, it is shown in previous works that this large number of orientations are absolutely needed when the grain boundary shearing process is simulated, because the obtained textures are relatively weak [47, 68]. The so-obtained texture is displayed in Fig. 11b. As can be seen by a visual comparison between the simulated and experimental textures, there is a great similarity. The direct correlation index confirms excellent agreement with a value of 91%. The main feature of the simulated texture is the dominance of the $B/\overline{B}$ components. This excellent result could be achieved due to the consideration of the grain boundary shearing process. The shear strength of the grain boundaries was set to 260 MPa in this simulation work. The contribution of grain boundary shearing to the total strain was estimated by the ratio of the average total grain boundary shear rate and the total shear rate (the latter is GB shear + normal slip). The simulations showed that 35% of the total deformation was produced by grain boundary shearing.

Effect of deformation twinning

To see the influence of twinning activity in the texture, simulations were carried out by implementing the simplified ATV twinning approach to the second stage of the two-step simulation. The numerical code permitted to control the amount of twinning by using only a fraction of the partial slip system family ($\{111\}\langle 112\rangle$) to form twins. Twinning was used only in the second step, because twinning scheme together with grain fragmentation modelling approach is not yet developed, hence it could not be considered below ε_{eq}= 4. Nevertheless, large effect of twinning was seen on the simulated textures, see in Fig. 11c. Just about 2% volume fraction corresponding to twins affected the texture so much that the direct correlation value was reduced from 91% to 61%. If twinning had been considered before ε_{eq}= 4.0, it would have added more effect on texture, decreasing the correlation value further. It can be said that two new features were seen as an effect of twinning: a higher intensity texture and significant rotation of certain ideal components (especially

the A and A_1^*).

Textures obtained by one-step simulations

In another separate simulation (in Taylor polycrystal model), only crystallographic slip was used from the beginning to the maximum strain (ε_{eq}= 6.5), along with the two slip system families $\{111\}\langle 110\rangle$ and $\{111\}\langle 112\rangle$. This Taylor polycrystal model gave a texture which was far from the experimental one, as can be seen in Fig. 11d. Especially, the intensity of the A_1^* component was lower than the experimental texture. The correlation index was only 65%, which can be qualified as a weak agreement with the experiment.

Grain fragmentation alone was employed into the Taylor polycrystal model without consideration of grain boundary shearing and deformation twinning. It led to a texture agreeing with 72% to the experimental one, which is a decent agreement, as shown in Fig. 11e. However, the overall intensity was too high, and the relative intensities of the components deviated significantly from the experimental ones (especially for the C component). But, the overall intensity and the intensity of A_1^* component improved in comparison to the Taylor simulation (Fig. 11d).

In another simulation, grain fragmentation was not employed, while only grain boundary shearing was utilized to simulate the texture, the result is shown in Fig. 11f. A high correlation value of 88% was achieved when 17% of the total deformation was produced by grain boundary shearing. The correlation value was close to that of the two-step approach (Fig. 11b). However, the overall ODF intensity was lower than in the experiment, and the C component was relatively high. In order to examine the differences between the two-step and grain boundary shearing-one-step simulations, the volume fractions of the ideal components for these cases are shown in Fig. 12.

4. Discussion

4.1. Correlation between microstructure and mechanical properties

The present contribution is a first attempt to acquire information on the behavior of a new HEA by employing HPCS. The main feature of HPCS is that it permits to deform a metal to very large strains and producing also the strain hardening curve for large deformation. The strain hardening capacity of the present HEA is remarkable; the initial yield stress of 0.16 GPa was increased to

more than 1.0 GPa at a maximum shear strain of 11. From the microstructure and mechanical properties, it is possible to infer that the main strengthening mechanisms in the HEA were strain hardening, grain refinement, and to a lesser extent deformation twins.

The SFE of a material is one of the properties that most impact the evolution of the microstructure and texture. The investigated HEA is estimated to have a SFE in the intermediate range of 40 to 45 mJm^{-2} [14]. The microstructure after the initial deformation (ε_{eq}= 1.8) consisted mostly of globular grains, shear bands, and deformation twins in low fraction. The change in grain shape at this stage can be attributed to the motion and re-arrangement of dislocations during plastic deformation. The observed grain refinement can also be explained by the same mechanism. Similar effect has been observed in severely plastically deformed high Mn steels with intermediate SFE (25 mJm^{-2}) [69].

Although the processed alloy had an intermediate SFE, the presence of twins within the microstructure evince that the critical stress to activate deformation twinning was reached; similar observations have been made in alloys with even higher SFE subjected to SPD [70, 71]. Whereas the volume fraction of twins in the microstructure was low after the initial deformation, the microstructure seems to indicate that twins played an important role, especially in the formation of shear bands. Indeed, one of the main mechanisms of shear band formation in fcc metals is the collapse of twin lamellae or layered dislocation arrangements [72] (Fig. 7a).

Nano-twins are known to increase the strength and enhance work hardening capability [11]. Deformation twins have been reported before in other fcc HEAs as well [11, 19, 73–75]. Twinning in fcc HEAs is due to the combined glide of a/6 ⟨112⟩ type Shockley partial dislocations on successive parallel ⟨111⟩ planes [73]. Skrotzki et al. [36] and Sonkusare et al. [37] examined the Cantor alloy and CoCuFeMnNi type HEA, respectively, after HPT deformation. Like in the present HEA, extreme grain refinement was observed in both of these HEAs at ambient temperature; down 24 nm after a shear strain of 20 in the Cantor alloy [36] and about 55 nm in the CoCuFeMnNi alloy after a shear strain of 157 [37]. In these works, grain refinement was correlated with the presence of deformation twins. This seems not to be the case in the present alloy because the volume fraction of deformation twins in the microstructure was low and the presence of shear bands seem to indicate the collapse of twins. Since the SFE of the studied HEA is in an intermediate range, grain refinement was produced mainly by dislocation driven grain fragmentation [70]. However,

the rate of grain fragmentation was relatively low in the initial part of deformation since the grain size remained large at about 32 μm after ε_{eq}= 1.8.

For larger deformations, the grain fragmentation proceeded further, with a higher rate; the average grain size decreased from 32 μm at ε_{eq} = 1.8, to 65 nm at ε_{eq} = 4.8 to finally 50 nm at ε_{eq} = 6.5, thus reaching a saturation at high strains. The grain fragmentation process is advancing through several structural elements that appear and develop during plastic deformation [76]. Dislocation cells are the first appearing elements, with progressively decreasing cell size [77, 78]. The dislocation walls are also becoming thinner with respect to the cell interiors [79]. Such a mechanism can actually explain the linear hardening stage (Stage IV) [80, 81]. Further grain fragmentation is caused by other type of dislocation walls which are common in all metals: the geometrically necessary boundaries (GNBs) [76], which are built up from the accumulation of geometrically necessary dislocations (GNDs). While the statistical dislocations are producing the overall deformation of the metal, the GNDs are appearing locally for accounting for the heterogeneities in the plastic deformation process. The GNDs produce lattice curvatures, then are gathering into GNB walls, forming a pattern similar to dislocation cells, at somewhat larger scale [82]. The disorientation across the GNBs is increasing progressively with strain because different slip systems are operating on the two sides of the GNB, leading to different lattice rotations [83]. The presented grain fragmentation mechanism is well accepted in the SPD community, and it was also the basis for the grain fragmentation model used in the present work [41].

It was observed for the present HEA alloy that its flow stress was nearly constant after a strain of about 2 (Fig. 10), which was concomitant with a nearly constant average grain size. This does not mean, however, that there was no further grain fragmentation during the nearly steady state stage. Two mechanisms can be responsible for the further refinement of the microstructure. The first is dynamic recovery, which has been observed [84] to promote refinement by partitioning the grains through the arrangement of dislocations. Furthermore, dynamic recovery can also lead to the development of the equiaxed microstructure and formation of high angle grain boundaries which are observed, for example, in Fig. 6 by the onset of continuous recrystallization. Continuous recrystallization is a recovery process [85], in which the dislocations accumulate into pre-existing grain boundaries leading to an increase of the disorientation. As this process continues, it culminates in the formation of high angle grain boundaries and equiaxed microstructures [86]. Continuous re-

crystallization has been usually observed for specimens after large cold deformation, in the case of the inhibition of boundary migration, and at low temperatures [87]. If continuous recrystallization occurs concomitantly with deformation it is usually referred to as continuous dynamic recrystallization (cDRX) [88, 89]. A recovery process (such as cDRX) may also explain the occurrence of GBS since as pointed out by Valiev et al. [90] the motion of dislocations along grain boundaries and their preferential annihilation at triple junction during recovery, result in grain boundary shearing. The present work also employed grain boundary shearing deformation mechanism in the modeling, justified by the very low grain size. The second mechanism that can influence microstructure evolution is dynamic recrystallization (DRX). DRX can also explain the observed shape-evolution that results in an equiaxed microstructure. Although at room and low temperatures thermally activated grain boundary motion is inhibited [91], owing to the high stresses acting in the material, migration can still occur under the action of a mechanical driving force [92, 93] since stress-driven grain boundaries seem to be more mobile (but still thermally activated) at low temperatures than curvature-driven boundaries [94]. In fact, it has been theorized that low-temperature stress driven grain boundary migration can initiate recrystallization [95]. Furthermore, it has been shown by Derby [96, 97] that when DRX is taking place, the point defined by shear-modulus-normalized flow stress and the burgers vector normalized grain size lies on single power-law in the steady state, irrespective of the material. The power-law exponent is about -0.6, but reduced to -0.5 for SPD materials [98]. For the present HEA alloy, the normalized stress - normalized grain size point is also coinciding with the Derby relation (see the Derby plot for SPD materials in Ref. [98]), providing another argument for the occurrence of DRX in this HEA alloy at room temperature. The DRX process is compensating the grain fragmentation process at very large strain, leading to a constant average grain size. The stress level becomes also constant, because the average value of the dislocation density is also stabilizing due to the DRX process.

The nanoindentation and microhardness values were kept increasing with strain, so the hardness did not saturate at high strain. Generally, for ultra-fined grain materials, the yield strength (σ_y) and hardness (HV) can be empirically related by $HV \approx 3 * \sigma_y$. However, the hardness to strength ratio is affected by the pile-up behaviors and the ability of the material to deform by shear [99]. Tian et al. [100] suggest empirical relation between the hardness and yield strength of HEAs. This is because HEAs are seen to deviate from the $HV \approx 3 * \sigma_y$ relation. For FCC HEAs the

strength-hardness relationship can be expressed as $HV = 2.63 * \sigma_y + 973$. Nevertheless, the empirical relations change with the composition of the alloy. In the present work, it was seen that the hardness values were more than three times the flow stress values. It is interesting to note that nanoindentation and microhardness values follow the same trend and the values were quite close, as illustrated in Fig. 10. This could be because of the ultra-fined grain size at higher strains, which makes nanoindentation similar to a microhardness test.

Nevertheless, owing to the low temperature of the deformation process, the intermediate SFE of the material and the high deformation strain, the dominant mechanisms seems to be dynamic recovery resulting in cDRX. However, at very high deformation strains, the activation of DRX cannot be completely excluded.

4.2. Texture evolution

The HPCS test imposed both compression and shear strains on the samples. Owing to a larger shear than compression component (see in Table 2), the obtained texture had a characteristic to a shear-type (Figs. 8, 11). The deformation texture was dominated by the $B/\overline{B}$ components (see Fig. 9a), all along the deformation process. The intensity of the texture components very well depends on the SFE of the alloy [101]. The SFE of the processed HEA is between 40 to 45 mJm^{-2}, which is an intermediate range. Generally, metals and alloys with high SFE have dominant C component whereas, medium and low SFE alloys tend to show $B/\overline{B}$ texture components [102] e.g. copper subjected to SPD by HPT [103], silver deformed by equal channel angular-extrusion (ECAE) [104], and CoCrFeMnNi deformed by HPT [36]. Typically, the $B/\overline{B}$ texture components dominate and C components are weaker. Hence, the processed alloy possesses also a $B/\overline{B}$ or brass-type shear texture.

The contribution of partial dislocations to the texture evolution can be significant [19]. When the grain size decreases, the dominance of partial dislocation slip leads to the formation of brass-type texture. In rolling of oxygen-free high thermal conductivity (OFHC) copper [105], the brass type texture was reproduced with polycrystal plasticity simulations, when the $\{111\}\langle 112\rangle$ type partial dislocations were added to the usual $\{111\}\langle 110\rangle$ slip systems. Other texture simulations also proved the contribution of partial dislocations to the deformation process [68, 106]. In all

these cases, the grain size was very small, even in nanometric range and the activity of partial dislocations emitted from the grain boundaries is also proved by atomistic-phase field dislocation dynamic simulations [107].

Apart from the intensity of the ideal components, the overall ODF intensity and texture index throughout the deformation was low. This low value is correlated to the deformation at large strains by grain boundary shearing. It is recognized by simulations, that the main effect of grain boundary shearing is a lowering of the texture intensity, that is, randomizing it [36]. In the grain boundary shearing process a localized shear parallel to a grain boundary does not create significant strain compatibility issues at the grain boundaries. Grain boundary shearing was also employed in the present simulation work and the same effects have been confirmed.

The dominance of $B/\overline{B}$ (brass-type) shear texture is due to the intermediate SFE and the possible contribution of partial dislocations in the processed HEA. The weak ODF intensity and texture index is correlated to the contribution of grain boundary shearing to the overall deformation process.

4.3. Polycrystal simulation approaches

The scalar direct correlation parameter (D) was used in the present work to evaluate quantitatively the agreement between the experimental and simulated textures. The highest D value was obtained when the simulation was done in two steps. In the first part, grain fragmentation was considered, while in the second one, the grain size was considered constant, but grain boundary shearing was activated. Under these conditions, an excellent agreement between simulations and experimental results was obtained (91%). This two-steps simulation technique can be fully justified by considering that in large strain deformation, the deformation mechanisms change as a function of strain. Grain fragmentation saturates at large strains thus, new deformation mechanisms become active [65]. Two of such mechanisms were used in the present work: grain boundary shearing and deformation by partial dislocations.

In order to demonstrate the effectiveness of the two-step modeling approach, one-step simulations were also done. They all led to lower agreement between the experimental and simulated textures. The best agreement in one-step simulation was the one where grain boundary shearing was

considered all along the deformation using the Taylor polycrystal deformation approach, without grain fragmentation (D = 88%). This result, however, should be considered just as a coincidence, because not all deformation mechanisms were considered in the simulation. To evaluate better the accuracy of the simulations, Fig. 12 shows a comparison of individual texture components determined experimentally and calculated in simulations. This figure shows a better agreement of the volume fraction of texture components for the two-steps approach. Furthermore, the sharpness of the two-step approach to experimental texture was better than in case of the grain boundary shearing-one-step approach. Interestingly, the uniform deformation mode assumed in the Taylor model is not far from the reality, for very small grain size ranges. This has been already pointed out in Ref. [108]. This is where grain refinement has another importance: in the grain shape effect. Namely, due to grain fragmentation, the geometrically assumed grain shape is not achieved in the material; very elongated grains are not visible in the microstructure. This is why the selection of the polycrystal model is turning to the Taylor model, not the self-consistent one. In several modeling, it has been found that the VPSC model with continuous geometrical updating of the grain shape cannot produce textures in agreement with the experiment in SPD [37, 65]. It has been also tried in the present case, however, in order to save space, the results are not shown, considering the very low direct correlation value of 48% with the experimental texture.

Finally, one has to examine also the effect of twinning on the textures. While nano-twins were visible in the microstructure, it turned out that a significant fraction of twinning could not be used in polycrystal modeling. Even by employing the ATV approach - which worked well in previous simulations, even in individual grains [54] - the direct correlation value was very low as soon as more than 2% volume fraction was produced by twinning (D = 61%). Thus, the contribution of twinning to texture development was found to be marginal. Nevertheless, twinning could have influenced the mechanical behavior of the studied HEA. As discussed in a previous section, at initial stages of deformations twin formation and their subsequent collapse results in shear band formation. At higher strains, because of grain refinement, other deformation mechanisms, such as grain boundary shearing became more prominent.

5. Conclusions

A non-equiatomic Al_6(CoFeMnNi) high-entropy alloy processed by induction melting and homogenization annealing was subjected to severe plastic deformation (SPD) using the high-pressure compressive shearing (HPCS) technique. The evolution of microstructure, texture, and mechanical properties were studied. Crystal plasticity simulations were essential to better understand and quantify the correlation between active deformation mechanisms and texture evolution. The polycrystal simulations were able to capture the experimental texture at high level of accuracy. After analyzing the experimental data and simulations, the following main conclusions can be made:

- High-pressure compressive shearing enabled exceptional refinement of the microstructure from coarse grain size ($\overline{d} \approx 170$ m) to ultra-fine equiaxed grains ($\overline{d} \approx 50$ nm) after an equivalent strain of 6.5. The average grain size was stabilized due to a balance between an always ongoing grain fragmentation process and a softening mechanism such as cDRX and possibly DRX at very high strains.

- Macro-texture analysis indicated the formation of an fcc brass-type shear texture with $B/\overline{B}$ $\{112\}\langle 110\rangle$ as the major component throughout the evolution. At lower strains, deformation twins collapsed to form shear bands and deformation induced nano-twins were seen at all stages of microstructure evolution. However, the latter were in low volume fraction, thus, not contributing significantly to the texture development.

- A special two-step Taylor-type polycrystal approach was formulated including grain fragmentation and grain boundary shearing. The comparison between the experimental and simulated textures approved the modeling by a high direct correlation value of 91%. The estimated contribution of grain boundary shearing to the overall deformation was 35%. This indicates that the main deformation mechanisms affecting texture development were: dislocation slide, grain fragmentation, and grain boundary shearing.

- Microstructure investigations substantiated the occurrence of deformation twinning resulting in shear bands at lower strains and nano-twins at all deformation stages. By including the all-twin variant approach in the polycrystal modeling, the simulations confirmed that the

volume fraction of the deformation induced nano-twins must have been less than 2% in the processed alloy.

Declaration of interests

The authors declare that they have no known competing financial interests or personal relationships that could have appeared to influence the work reported in this paper.

Acknowledgements

Surya N. Kumaran thanks Dr. Viet V. Qu, LEM3 for the help during the HPCS experiments, Dr. Laurent Peltier, LEM3 for the help during casting, Dr. Yudong Zhang, LEM3 for the extensive help during the TEM and FSD imaging, and Dr. Jean-Sébastien Lecomte, LEM3 for his help with expertise in nanoindentation.

The funding support from Lorraine University of Excellence (LUE) (PFI: R01PJIYX) is acknowledged by Surya N. Kumaran.

This work was supported by the French State through the program "Investment in the future" operated by the National Research Agency (ANR) and referenced by ANR-11-LABX-0008-01 (LabEx DAMAS).

Laszlo S. Toth acknowledges the support received for this research from the University of Miskolc, from the action Developments aimed at increasing social benefits deriving from more efficient exploitation and utilization of domestic subsurface natural resources" project supported by the Ministry of Innovation and Technology from the National Research, Development and Innovation Fund according to the Grant Contract issued by the National Research, Development and Innovation Office (Grant Contract reg. nr.: TKP-17-1/PALY-2020)".

Christian Haase thanks the Deutsche Forschungsgemeinschaft (DFG, German Research Foundation) for the support of the depicted research within the priority programme 2006 CCA HEA (project-ID 388166069) and the support of the German Federal Ministry of Education and Research (BMBF) within the NanoMatFutur project MatAM - Design of additively manufactured high-performance alloys for automotive applications (Project ID.:03XP0264).

References

[1] B. Murty, J.-W. Yeh, S. Ranganathan, P. Bhattacharjee, High-Entropy Alloys, second edition Edition, Elsevier, 2019. doi:10.1016/C2017-0-03317-7.
URL https://www.elsevier.com/books/high-entropy-alloys/murty/978-0-12-816067-1

[2] M. C. Gao, J. W. Yeh, P. K. Liaw, Y. Zhang, High-entropy alloys: Fundamentals and applications, Springer, 2016. doi:10.1007/978-3-319-27013-5.

[3] B. Cantor, I. T. Chang, P. Knight, A. Vincent, Microstructural development in equiatomic multicomponent alloys, Materials Science and Engineering A 375-377 (2004) 213–218. doi:10.1016/j.msea.2003.10.257.

[4] J. W. Yeh, S. K. Chen, S. J. Lin, J. Y. Gan, T. S. Chin, T. T. Shun, C. H. Tsau, S. Y. Chang, Nanostructured high-entropy alloys with multiple principal elements: Novel alloy design concepts and outcomes, Advanced Engineering Materials 6 (2004) 299–303. doi:10.1002/adem.200300567.

[5] D. B. Miracle, O. N. Senkov, A critical review of high entropy alloys and related concepts, Acta Materialia 122 (2017) 448–511. doi:10.1016/j.actamat.2016.08.081.

[6] O. N. Senkov, J. D. Miller, D. B. Miracle, C. Woodward, Accelerated exploration of multi-principal element alloys for structural applications, Calphad: Computer Coupling of Phase Diagrams and Thermochemistry 50 (2015) 32–48. doi:10.1016/j.calphad.2015.04.009.

[7] C. Haase, F. Tang, M. B. Wilms, A. Weisheit, B. Hallstedt, Combining thermodynamic modeling and 3D printing of elemental powder blends for high-throughput investigation of high-entropy alloys Towards rapid alloy screening and design, Materials Science and Engineering A 688 (January) (2017) 180–189. doi:10.1016/j.msea.2017.01.099.

[8] E. P. George, W. A. Curtin, C. C. Tasan, High entropy alloys: A focused review of mechanical properties and deformation mechanisms, Acta Materialia 188 (2020) 435–474. doi:10.1016/j.actamat.2019.12.015.

[9] Z. Tang, M. C. Gao, H. Diao, T. Yang, J. Liu, T. Zuo, Y. Zhang, Z. Lu, Y. Cheng, Y. Zhang, K. A. Dahmen, P. K. Liaw, T. Egami, Aluminum alloying effects on lattice types, microstructures, and mechanical behavior of high-entropy alloys systems, JOM 65 (12) (2013) 1848–1858. doi:10.1007/s11837-013-0776-z.

[10] C. J. Tong, M. R. Chen, S. K. Chen, J. W. Yeh, T. T. Shun, S. J. Lin, S. Y. Chang, Mechanical performance of the AlxCoCrCuFeNi high-entropy alloy system with multiprincipal elements, Metallurgical and Materials Transactions A: Physical Metallurgy and Materials Science 36 (5) (2005) 1263–1271. doi:10.1007/s11661-005-0218-9.

[11] W. Li, D. Xie, D. Li, Y. Zhang, Y. Gao, P. K. Liaw, Mechanical behavior of high-entropy alloys, Progress in Materials Science 118 (2021) 100777. doi:10.1016/j.pmatsci.2021.100777.

[12] F. Kies, M. Noori, S. Ewald, J. H. Schleifenbaum, B. Hallstedt, C. Haase, Thermodynamics, microstructure evolution and mechanical properties of al- and c-added cofemnni multi-principal element alloys, Materials and Design 224. doi:10.1016/j.matdes.2022.111368.

[13] A. Saeed-Akbari, J. Imlau, U. Prahl, W. Bleck, Derivation and variation in composition-dependent stacking fault energy maps based on subregular solution model in high-manganese steels, Metallurgical and Materials Transactions A: Physical Metallurgy and Materials Science 40 (2009) 3076–3090. doi:10.1007/s11661-009-0050-8.

[14] F. Kies, Y. Ikeda, S. Ewald, J. H. Schleifenbaum, B. Hallstedt, F. Körmann, C. Haase, Combined Al and C alloying enables mechanism-oriented design of multi-principal element alloys: Ab initio calculations and experiments, Scripta Materialia 178 (2020) 366–371. doi:10.1016/j.scriptamat.2019.12.004.

[15] A. Karati, K. Guruvidyathri, V. S. Hariharan, B. S. Murty, Thermal stability of AlCoFeMnNi high-entropy alloy, Scripta Materialia 162 (2019) 465–467. doi:10.1016/j.scriptamat.2018.12.017.

[16] W. H. Liu, Y. Wu, J. Y. He, T. G. Nieh, Z. P. Lu, Grain growth and the hall-petch relationship in a high-entropy fecrnicomn alloy, Scripta Materialia 68 (2013) 526–529. doi:10.1016/j.scriptamat.2012.12.002.

[17] B. Gwalani, V. Soni, M. Lee, S. A. Mantri, Y. Ren, R. Banerjee, Optimizing the coupled effects of hall-petch and precipitation strengthening in a al0.3cocrfeni high entropy alloy, Materials and Design 121 (2017) 254–260. doi:10.1016/j.matdes.2017.02.072.

[18] Y. C. Huang, C. H. Su, S. K. Wu, C. Lin, A study on the hall-petch relationship and grain growth kinetics in fcc-structured high/medium entropy alloys, Entropy 21. doi:10.3390/e21030297.

[19] G. D. Sathiaraj, A. Pukenas, W. Skrotzki, Texture formation in face-centered cubic high-entropy alloys, Journal of Alloys and Compounds 826 (2020) 154183. doi:10.1016/j.jallcom.2020.154183.

[20] B. B. Straumal, R. Kulagin, B. Baretzky, N. Y. Anisimova, M. V. Kiselevskiy, L. Klinger, P. B. Straumal, O. A. Kogtenkova, R. Z. Valiev, Severe Plastic Deformation and Phase Transformations in High Entropy Alloys: A Review, Crystals 12 (1) (2022) 54. doi:10.3390/cryst12010054.

[21] Y. Estrin, A. Vinogradov, Extreme grain refinement by severe plastic deformation: A wealth of challenging science, Acta Materialia 61 (3) (2013) 782–817. doi:10.1016/j.actamat.2012.10.038.

[22] L. S. Toth, C. Gu, Ultrafine-grain metals by severe plastic deformation, Materials Characterization 92 (2014) 1–14. doi:10.1016/j.matchar.2014.02.003.

[23] P. P. Bhattacharjee, G. D. Sathiaraj, M. Zaid, J. R. Gatti, C. Lee, C. W. Tsai, J. W. Yeh, Microstructure and texture evolution during annealing of equiatomic CoCrFeMnNi high-entropy alloy, Journal of Alloys and Compounds 587 (2014) 544–552. doi:10.1016/j.jallcom.2013.10.237.

[24] G. D. Sathiaraj, P. P. Bhattacharjee, Effect of cold-rolling strain on the evolution of annealing texture of equiatomic CoCrFeMnNi high entropy alloy, Materials Characterization 109 (2015) 189–197. doi:10.1016/j.matchar.2015.09.027.

[25] C. Haase, L. A. Barrales-Mora, Influence of deformation and annealing twinning on the microstructure and texture evolution of face-centered cubic high-entropy alloys, Acta Materialia 150 (2018) 88–103. doi:10.1016/j.actamat.2018.02.048.

[26] B. Schuh, F. Mendez-Martin, B. Völker, E. P. George, H. Clemens, R. Pippan, A. Hohenwarter, Mechanical properties, microstructure and thermal stability of a nanocrystalline CoCrFeMnNi high-entropy alloy after severe plastic deformation, Acta Materialia 96 (2015) 258–268. doi:10.1016/j.actamat.2015.06.025.

[27] Y. Bian, Y. Li, N. Zhang, Z. Feng, X. Wang, B. Zhang, Y. Cai, L. Lu, S. Chen, X. Yao, S. Luo, Ultrafast severe plastic deformation in high-entropy alloy Al0.1CoCrFeNi via dynamic equal channel angular pressing, Materials Science and Engineering: A (2020) 132540doi:10.1016/j.msea.2022.143221.

[28] V. M. Segal, Materials processing by simple shear, Materials Science and Engineering A 197 (2) (1995) 157–164. doi:10.1016/0921-5093(95)09705-8.

[29] A. P. Zhilyaev, T. G. Langdon, Using high-pressure torsion for metal processing: Fundamentals and applications, Progress in Materials Science 53 (6) (2008) 893–979. doi:10.1016/j.pmatsci.2008.03.002.

[30] H. Shahmir, T. Mousavi, J. He, Z. Lu, M. Kawasaki, T. G. Langdon, Microstructure and properties of a CoCrFeNiMn high-entropy alloy processed by equal-channel angular pressing, Materials Science and Engineering A 705 (2017) 411–419. doi:10.1016/j.msea.2017.08.083.

[31] L. S. Toth, V. Q. Vu, S. S. Dhinwal, Y. Zhao, R. Massion, C. Chen, C. F. Davis, T. C. Lowe, The mechanics of High Pressure Compressive Shearing with application to ARMCO® steel, Materials Characterization 154 (2019) 127–137. doi:10.1016/j.matchar.2019.05.039.

[32] T. Fujioka, Z. Horita, Development of high-pressure sliding process for microstructural refinement of rectangular metallic sheets, Materials Transactions 50 (2009) 930–933. doi:10.2320/matertrans.MRP2008445.

[33] S. Lee, K. Tazoe, I. F. Mohamed, Z. Horita, Strengthening of aa7075 alloy by processing with high-pressure sliding (hps) and subsequent aging, Materials Science and Engineering A 628 (2015) 56–61. doi:10.1016/j.msea.2015.01.026.

[34] J. Gubicza, P. T. Hung, M. Kawasaki, J. K. Han, Y. Zhao, Y. Xue, J. L. Lábár, Influence of severe plastic deformation on the microstructure and hardness of a CoCrFeNi high-entropy alloy: A comparison with CoCrFeNiMn, Materials Characterization 154 (2019) 304–314. doi:10.1016/j.matchar.2019.06.015.

[35] A. Heczel, M. Kawasaki, J. L. Lbr, J. il Jang, T. G. Langdon, J. Gubicza, Defect structure and hardness in nanocrystalline cocrfemnni high-entropy alloy processed by high-pressure torsion, Journal of Alloys and Compounds 711 (2017) 143–154. doi:10.1016/j.jallcom.2017.03.352.

[36] W. Skrotzki, A. Pukenas, E. Odor, B. Joni, T. Ungar, B. Völker, A. Hohenwarter, R. Pippan, E. P. George, Microstructure, Texture, and Strength Development during High-Pressure Torsion of CrMnFeCoNi High-Entropy Alloy, Crystals 10 (4) (2020) 336. doi:10.3390/cryst10040336.

[37] R. Sonkusare, K. Biswas, N. Al-Hamdany, H. G. Brokmeier, R. Kalsar, N. Schell, N. P. Gurao, A critical evaluation of microstructure-texture-mechanical behavior heterogeneity in high pressure torsion processed CoCuFeMnNi high entropy alloy, Materials Science and Engineering A 782 (2020) 139187. doi:10.1016/j.msea.2020.139187.

[38] P. W. Trimby, Orientation mapping of nanostructured materials using transmission Kikuchi diffraction in the scanning electron microscope, Ultramicroscopy 120 (2012) 16–24. doi:10.1016/j.ultramic.2012.06.004.

[39] M. Schaffer, B. Schaffer, Q. Ramasse, Sample preparation for atomic-resolution STEM at

low voltages by FIB, Ultramicroscopy 114 (2012) 62–71. doi:10.1016/j.ultramic.2012.01.005.

[40] B. Beausir, J. Fundenberger, Analysis Tools for Electron and X-ray diffraction, ATEX-software, Universit de Lorraine - Metz (2017).
URL www.atex-software.eu

[41] L. S. Tóth, Y. Estrin, R. Lapovok, C. Gu, A model of grain fragmentation based on lattice curvature, Acta Materialia 58 (5) (2010) 1782–1794. doi:10.1016/j.actamat.2009.11.020.

[42] S. R. Kalidindi, C. A. Bronkhorst, L. Anand, Crystallographic texture evolution in bulk deformation processing of fcc metals, J. Mech. Phys. Solids 40 (1992) 537–569. doi:10.1016/0022-5096(92)80003-9.

[43] Y. Zhou, K. W. Neale, L. S. Tóth, A modified model for simulating latent hardening during the plastic deformation of rate-dependent FCC polycrystals, International Journal of Plasticity 9 (8) (1993) 961–978. doi:10.1016/0749-6419(93)90061-T.

[44] R. Hill, Generalized constitutive relations for incremental deformation of metal crystals by multislip, J. Mech. Phys. Solids 14 (1966) 95–102. doi:10.1016/0022-5096(66)90040-8.

[45] S. K. Sahoo, S. S. Dhinwal, V. Q. Vu, L. S. Toth, A new macroscopic strain hardening function based on microscale crystal plasticity and its application in polycrystal modeling, Materials Science and Engineering A 823 (2021) 141634. doi:10.1016/j.msea.2021.141634.

[46] S. K. Sahoo, L. S. Toth, S. Biswas, An analytical model to predict strain-hardening behaviour and twin volume fraction in a profoundly twinning magnesium alloy, International Journal of Plasticity 119 (2019) 273–290. doi:10.1016/j.ijplas.2019.04.007.

[47] Y. Zhao, L. S. Toth, R. Massion, W. Skrotzki, Role of Grain Boundary Sliding in Texture Evolution for Nanoplasticity, Advanced Engineering Materials 1700212 (2017) 1–9. doi:10.1002/adem.201700212.

[48] J. Pan, R. J. Rice, Rate sensitivity of plastic flow and implications for yield-surface vertices, Int. J. Solids Structures 19 (ll) (1983) 973–987. doi:10.1016/0020-7683(83)90023-9.

[49] D. Peirce, R. Asaro, A. Needleman, Material rate dependence and localized deformation in crystalline solids, Acta Metallurgica 31 (12) (1983) 1951–1976. doi:10.1016/0001-6160(83)90014-7.

[50] R. J. Asaro, A. Needleman, Texture development and strain hardening in rate dependent polycrystals, Acta Metall. 33 (1984) 923–953. doi:10.1016/0001-6160(85)90188-9.

[51] J. W. Hutchinson, Bounds and self-consistent estimates for creep of polycrystalline materials, Proc. R. Soc. Lond. 348 (1652) (1976) 101–127. doi:https://doi.org/10.1098/rspa.1976.0027.

[52] L. Tóth, J. Jonas, K. Neale, Comparison of the minimum plastic spin and rate sensitive slip theories for loading of symmetrical crystal orientations, Proc. R. Soc. Lond. 427 (1872) (1990) 201–219. doi:10.1098/rspa.1990.0008.

[53] G. Canova, C. Fressengeas, A. Molinari, U. Kocks, Effect of rate sensitivity on slip system and lattice rotation, Acta Metallurgica 36 (8) (1988) 1961–1970. doi:https://doi.org/10.1016/0001-6160(88)90298-2.

[54] S. K. Sahoo, S. Biswas, L. S. Toth, P. C. Gautam, B. Beausir, Strain hardening, twinning and texture evolution in magnesium alloy using the all twin variant polycrystal modelling approach, International Journal of Plasticity 128 (2020) 102660. doi:10.1016/j.ijplas.2020.102660.

[55] C. F. Gu, L. S. Tóth, Polycrystal modeling of tensile twinning in a Mg alloy during cyclic loading, Scripta Materialia 67 (7-8) (2012) 673–676. doi:10.1016/j.scriptamat.2012.07.008.

[56] L. S. Toth, C. Haase, R. Allen, R. Lapovok, D. A. Molodov, M. Cherkaoui, H. E. Kadiri, Modeling the effect of primary and secondary twinning on texture evolution during severe plastic deformation of a twinning-induced plasticity steel, Materials 11 (5) (2018) 863. doi:10.3390/ma11050863.

[57] C. F. Gu, L. S. Toth, M. Hoffman, Twinning effects in a polycrystalline magnesium alloy under cyclic deformation, Acta Materialia 62 (2014) 212–224. doi:10.1016/j.actamat.2013.09.048.

[58] C. N. Tom, R. A. Lebensohn, U. F. Kocks, A model for texture development dominated by deformation twinning: Application to zirconium alloys, Actametall. mater 39 (1991) 2667–2680. doi:10.1016/0956-7151(91)90083-D.

[59] R. R. Keller, R. H. Geiss, Transmission EBSD from 10 nm domains in a scanning electron microscope, Journal of Microscopy 245 (3) (2012) 245–251. doi:10.1111/j.1365-2818.2011.03566.x.

[60] R. R. Eleti, T. Bhattacharjee, A. Shibata, N. Tsuji, Unique deformation behavior and microstructure evolution in high temperature processing of HfNbTaTiZr refractory high entropy alloy, Acta Materialia 171 (2019) 132–145. doi:10.1016/j.actamat.2019.04.018.
URL https://doi.org/10.1016/j.actamat.2019.04.018

[61] H. Wang, R. Li, M. Zhou, J. Cedelle, Z. Huang, Q. Wang, Grain boundary sliding mechanism in plastic deformation of nano-grained yag transparent ceramics: Generalized self-consistent model and nanoindentation experimental validation, Journal of the European Ceramic Society 37 (2017) 2705–2715. doi:10.1016/j.jeurceramsoc.2017.02.010.

[62] L. S. Toth, P. Gilormini, J. J. Jonas, Effect of rate sensitivity on the stability of torsion textures, Acta Metallurgica 36 (12) (1988) 3077–3091. doi:10.1016/0001-6160(88)90045-4.

[63] H. J. Bunge, Texture Analysis in Materials Science, Butterworth and Co, 1969. doi:10.1016/C2013-0-11769-2.

[64] W. C. Oliver, G. M. Pharr, Measurement of hardness and elastic modulus by instrumented indentation: Advances in understanding and refinements to methodology, Journal of Materials Research 19 (2004) 3–20. doi:10.1557/JMR.2004.19.1.3.

[65] W. Skrotzki, A. Eschke, B. Jóni, T. Ungár, L. S. Tóth, Y. Ivanisenko, L. Kurmanaeva, New experimental insight into the mechanisms of nanoplasticity, Acta Materialia 61 (19) (2013) 7271–7284. doi:10.1016/j.actamat.2013.08.032.

[66] Y. T. Zhu, X. Z. Liao, X. L. Wu, Deformation twinning in nanocrystalline materials, Progress in Materials Science 57 (1) (2012) 1–62. doi:10.1016/j.pmatsci.2011.05.001.

[67] V. Q. Vu, L. S. Toth, Y. Beygelzimer, R. Kulagin, A. H. Kobaissy, Modeling of Crystallographic Texture in Plastic Flow Machining, Advanced Engineering Materials 1900661 (2019) 1–10. doi:10.1002/adem.201900661.

[68] L. S. Toth, W. Skrotzki, Y. Zhao, A. Pukenas, C. Braun, R. Birringer, Revealing grain boundary sliding from textures of a deformed nanocrystalline Pd-Au alloy, Materials 11 (2) (2018) 1–8. doi:10.3390/ma11020190.

[69] C. Haase, L. A. Barrales-Mora, From high-manganese steels to advanced high-entropy alloys, Metals 9 (7) (2019) 726. doi:10.3390/met9070726.

[70] C. Haase, O. Kremer, W. Hu, T. Ingendahl, R. Lapovok, D. A. Molodov, Equal-channel angular pressing and annealing of a twinning-induced plasticity steel: Microstructure, texture, and mechanical properties, Acta Materialia 107 (2016) 239–253. doi:10.1016/j.actamat.2016.01.056.

[71] X. Z. Liao, Y. H. Zhao, S. G. Srinivasan, Y. T. Zhu, R. Z. Valiev, D. V. Gunderov, Deformation twinning in nanocrystalline copper at room temperature and low strain rate, Applied Physics Letters 84 (2004) 592–594. doi:10.1063/1.1644051.

[72] K. Morii, H. Mecking, Y. Nakayama, Development of shear bands in f.c.c. single crystals, Acta. Metall. 33 (1985) 379–386. doi:10.1016/0001-6160(85)90080-X.

[73] H. Y. Diao, R. Feng, K. A. Dahmen, P. K. Liaw, Fundamental deformation behavior in high-entropy alloys: An overview, Current Opinion in Solid State and Materials Science 21 (5) (2017) 252–266. doi:10.1016/j.cossms.2017.08.003.

[74] T. S. Reddy, I. S. Wani, T. Bhattacharjee, S. R. Reddy, R. Saha, P. P. Bhattacharjee, Severe plastic deformation driven nanostructure and phase evolution in a Al0.5CoCrFeMnNi dual phase high entropy alloy, Intermetallics 91 (2017) 150–157. doi:10.1016/j.intermet.2017.09.002.

[75] M. Liu, S. Zhang, F. Li, Y. Luo, Y. Yao, H. Zhang, Z. Wang, L. Wang, Z. Wang, Tailoring the strength and ductility of Al0.25CoCrFeNi high entropy alloy through cryo-rolling and annealing, Materials Science and Engineering: A 826 (2021) 141964. doi:10.1016/j.msea.2021.141964.

[76] D. A. Hughes, N. Hansen, Deformation structures developing on fine scales, Philosophical Magazine 83 (2003) 3871–3893. doi:10.1080/14786430310001605560.

[77] D. Kuhlmann-Wilsdorf, Theory of plastic deformation:-properties of low energy dislocation structures, Materials Science and Engineering A 113 (1989) 1–41. doi:10.1016/0921-5093(89)90290-6.

[78] D. L. Holt, Dislocation cell formation in metals, Journal of Applied Physics 41 (1970) 3197–3201. doi:10.1063/1.1659399.

[79] M. Mller, M. Zehetbauer, A. Borbely, T. Ungar, Dislocation density and long range internal stresses in heavily cold worked cu measured by x-ray line broadening, International Journal of Materials Research 86 (1995) 827–831. doi:10.1515/ijmr-1995-861205.

[80] Y. Estrin, L. S. Toth, A. Molinari, Y. Brechet, A dislocation based model for all hardening stages in large strain deformation, Acta mater. 46 (1998) 5509–5522. doi:10.1016/S1359-6454(98)00196-.

[81] L. S. Tth, A. Molinari, Y. Estrin, Strain hardening at large strains as predicted by dislocation based polycrystal plasticity model, Journal of Engineering Materials and Technology 124 (2002) 71–77. doi:10.1115/1.1421350.

[82] C. F. Gu, L. S. Tth, B. Beausir, Modeling of large strain hardening during grain refinement, Scripta Materialia 66 (2012) 250–253. doi:10.1016/j.scriptamat.2011.11.002.

[83] W. Pantleon, On the statistical origin of disorientations in dislocation structures, Acta. Mater. 46 (1998) 451–456. doi:10.1016/S1359-6454(97)00286-3.

[84] Z. Liao, M. Polyakov, O. G. Diaz, D. Axinte, G. Mohanty, X. Maeder, J. Michler, M. Hardy, Grain refinement mechanism of nickel-based superalloy by severe plastic deformation - mechanical machining case, Acta Materialia 180 (2019) 2–14. doi:10.1016/j.actamat.2019.08.059.

[85] G. Gottstein, Physical foundations of materials science, Vol. 42, 2005. doi:10.5860/choice.42-2828.

[86] B. Eghbali, Effect of strain rate on the microstructural development through continuous dynamic recrystallization in a microalloyed steel, Materials Science and Engineering A 527 (2010) 3402–3406. doi:10.1016/j.msea.2010.01.077.

[87] S. V. Murty, S. Torizuka, K. Nagai, T. Kitai, Y. Kogo, Dynamic recrystallization of ferrite during warm deformation of ultrafine grained ultra-low carbon steel, Scripta Materialia 53 (2005) 763–768. doi:10.1016/j.scriptamat.2005.05.027.

[88] A. Karmakar, R. D. Misra, S. Neogy, D. Chakrabarti, Development of ultrafine-grained dual-phase steels: Mechanism of grain refinement during intercritical deformation, Metallurgical and Materials Transactions A 44 (2013) 4106–4118. doi:10.1007/s11661-013-1757-0.

[89] T. Sakai, A. Belyakov, R. Kaibyshev, H. Miura, J. J. Jonas, Dynamic and post-dynamic recrystallization under hot, cold and severe plastic deformation conditions, Progress in Materials Science 60 (2014) 130–207. doi:10.1016/j.pmatsci.2013.09.002.

[90] R. Z. Valiev, Y. V. Ivanisenko, E. F. Rauch, B. Baudelet, Structure and deformation behaviour of armco iron subjected to severe plastic deformation, Acta. mater. 44 (1996) 4705–4712. doi:10.1016/S1359-6454(96)00156-5.

[91] G. Gottstein, L. S. Shvindlerman, Grain Boundary Migration in Metals : Thermodynamics, Kinetics, Applications, Second Edition, CRC Press, 2009. doi:10.1201/9781420054361.

[92] T. Gorkaya, D. A. Molodov, G. Gottstein, Stress-driven migration of symmetrical 100 tilt grain boundaries in al bicrystals, Acta Materialia 57 (18) (2009) 53965405. doi:10.1016/j.actamat.2009.07.036.

[93] G. Gottstein, D. A. Molodov, L. S. Shvindlerman, D. J. Srolovitz, M. Winning, Grain boundary migration: misorientation dependence, Current Opinion in Solid State and Materials Science (2001) 9–14doi:10.1016/S1359-0286(00)00030-9.

[94] D. A. Molodov, T. Gorkaya, G. Gottstein, Dynamics of grain boundaries under applied mechanical stress, Journal of Materials Science 46 (2011) 4318–4326. doi:10.1007/s10853-010-5233-6.

[95] J. W. Cahn, Y. Mishin, Recrystallization initiated by low-temperature grain boundary motion coupled to stress, International Journal of Materials Research 100 (2013) 510–515. doi:10.3139/146.110066.

[96] B. Derby, The dependence of grain size on stress during dynamic recrystallisation, Acta metall, mater 39 (1991) 955–962. doi:10.1016/0956-7151(91)90295-C.

[97] B. Derby, Dynamic recrystallisation: The steady state grain size 27 (1992) 1581–1586. doi:10.1016/0956-716X(92)90148-8.

[98] A. Pougis, L. S. Toth, J. J. Fundenberger, A. Borbely, Extension of the derby relation to metals severely deformed to their steady-state ultrafine-grain size, Scripta Materialia 72-73 (2014) 59–62. doi:10.1016/j.scriptamat.2013.10.020.

[99] P. Zhang, S. X. Li, Z. F. Zhang, General relationship between strength and hardness, Materials Science and Engineering A 529 (2011) 62–73. doi:10.1016/j.msea.2011.08.061.

[100] Y. Tian, L. Li, J. Li, Y. Yang, S. Li, G. Qin, Correlating strength and hardness of high-entropy alloys, Advanced Engineering Materials 23. doi:10.1002/adem.202001514.

[101] R. Z. Valiev, T. G. Langdon, Achieving exceptional grain refinement through severe plastic deformation: New approaches for improving the processing technology, Metallurgical and Materials Transactions A 42 (10) (2011) 2942–2951. doi:10.1007/s11661-010-0556-0.

[102] H. Azzeddine, D. Bradai, T. Baudin, T. G. Langdon, Texture evolution in high-pressure torsion processing, Progress in Materials Science 125 (2022) 1–52. doi:10.1016/j.pmatsci.2021.100886.

[103] N. A. Enikeev, E. Schafler, M. Zehetbauer, I. V. Alexandrov, Observations of Texture in Large Scale HPT-Processed Cu, Materials Science Forum 584-586 (2008) 367–374. doi:10.4028/www.scientific.net/MSF.584-586.367.

[104] S. Suwas, L. S. Tth, J. J. Fundenberger, A. Eberhardt, W. Skrotzki, Evolution of crystallographic texture during equal channel angular extrusion of silver, Scripta Materialia 49 (2003) 1203–1208. doi:10.1016/j.scriptamat.2003.08.011.

[105] C. F. Gu, M. Hoffman, L. S. Toth, Y. D. Zhang, Grain size dependent texture evolution in severely rolled pure copper, Materials Characterization 101 (2015) 180–188. doi:10.1016/j.matchar.2015.02.003.

[106] L. Li, T. Ungr, L. S. Toth, W. Skrotzki, Y. D. Wang, Y. Ren, H. Choo, Z. Fogarassy, X. T. Zhou, P. K. Liaw, Shear-coupled grain growth and texture development in a nanocrystalline ni-fe alloy during cold rolling, Metallurgical and Materials Transactions A 47 (2016) 6632–6644. doi:10.1007/s11661-016-3753-7.

[107] A. Hunter, I. J. Beyerlein, Unprecedented grain size effect on stacking fault width, APL Materials 1 (2013) 032109. doi:10.1063/1.4820427.

[108] L. S. Toth, C. F. Gu, B. Beausir, J. Fundenberger, M. Hoffman, Geometrically necessary dislocations favor the taylor uniform deformation mode in ultra- fine-grained polycrystals, Acta Materialia 117 (2016) 35–42. doi:10.1016/j.actamat.2016.06.062.

Table 1: Chemical composition of the processed HEA.

Element	Al	Co	Fe	Mn	Ni
wt. %	3.00	25.03	23.72	23.33	24.93

Table 2: Initial parameters and calculated values of the single-pass HPCS testing on Al_6(CoFeMnNi) HEA.

Sample number	1	2	3
Initial thickness (mm)	2.49	2.00	1.47
Initial length (mm)	10.26	9.68	9.86
Displacement (mm)	5.57	10.50	10.56
Thickness at the end of the pass (mm)	1.58	1.25	0.75
Shear strain	2.85	8.12	11.03
Equivalent strain	1.75	4.80	6.50

Table 3: Ideal shear orientations for fcc metals and alloys along with its miller indices and Euler angles [62].

Orientation	Miller indices	Euler angles		
		φ_1	ϕ	φ_2
A	$\left(11\bar{1}\right)[1\bar{1}0]$	0	35.26	45
$\bar{A}$	$\left(\bar{1}\bar{1}1\right)[\bar{1}10]$	180	35.26	45
A_1^*	$\left(11\bar{1}\right)[112]$	35.26	45	0
A_2^*	$\left(1\bar{1}1\right)[\bar{2}\bar{1}1]$	144.74	45	0
B	$\left(11\bar{2}\right)[1\bar{1}0]$	0	54.74	45
$\bar{B}$	$\left(\bar{1}\bar{1}2\right)[\bar{1}10]$	180	54.75	45
C	$(100)[0\bar{1}1]$	90	45	0

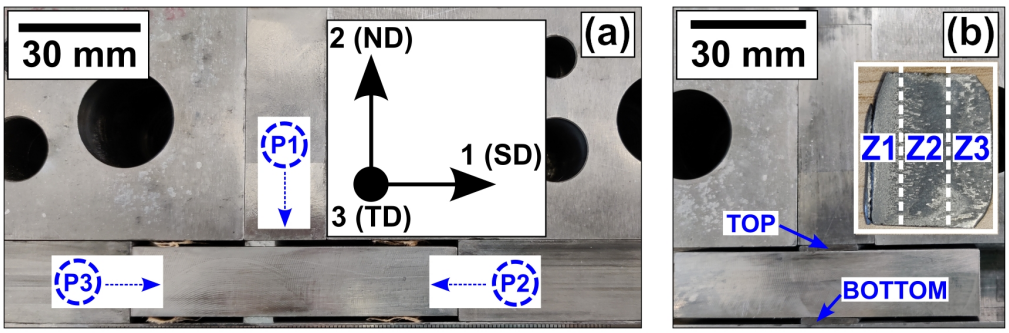

Figure 1: The HPCS installation (a) before testing, and (b) after deformation (subset: picture of a deformed sample).

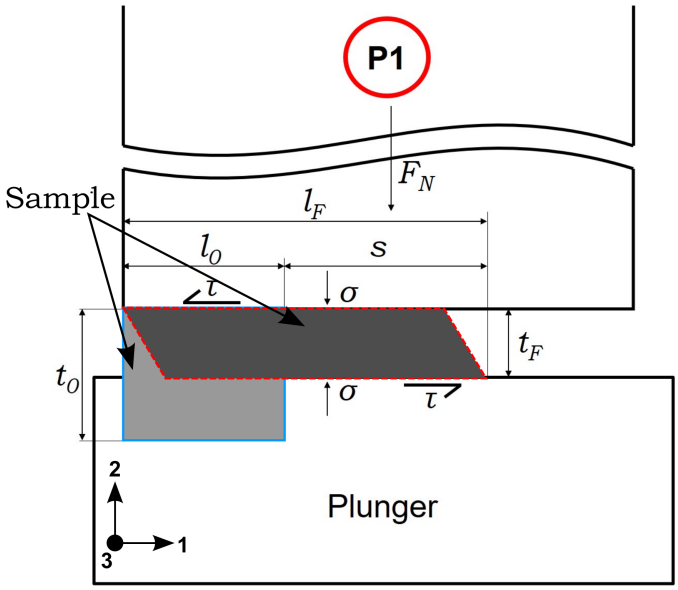

Figure 2: Schematic diagram presenting the dimensions and forces associated with HPCS [31].

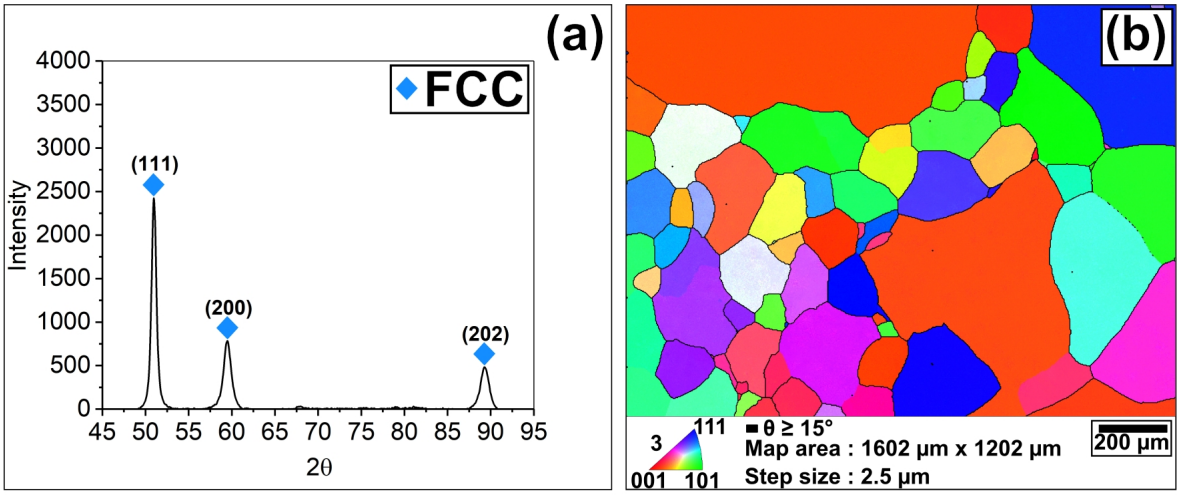

Figure 3: XRD pattern of Al_6(CoFeMnNi) HEA obtained after homogenization annealing at 1423 K for 2 h, and (b) EBSD- IPF map of the initial sample.

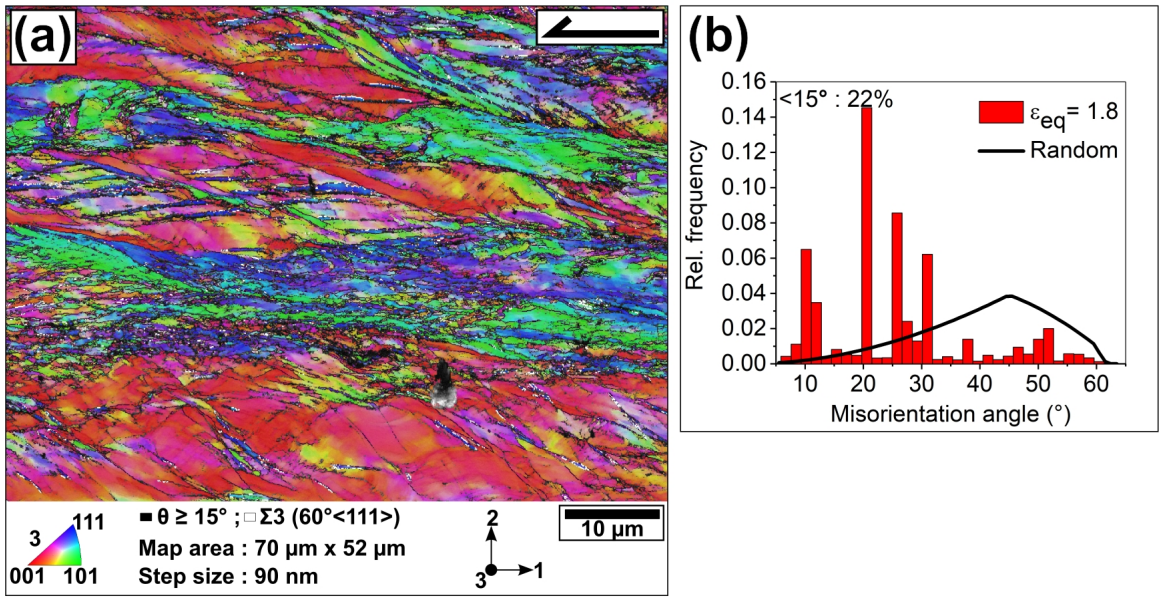

Figure 4: (a) EBSD- IPF map of Al_6(CoFeMnNi) after HPCS deformation at ε_{eq}= 1.8 and (b) neighbor-to-neighbor misorientation distribution.

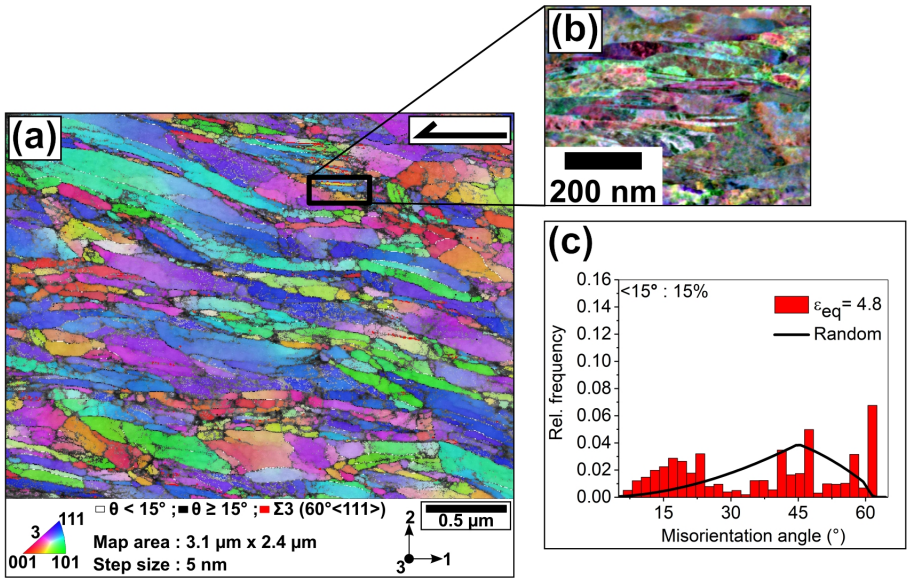

Figure 5: (a) TKD- IPF map of Al_6(CoFeMnNi) after HPCS deformation at ε_{eq}= 4.8, (b) FSD image confirming nano-twins at a specific spot (black rectangular box), and (c) neighbor-to-neighbor misorientation distribution.

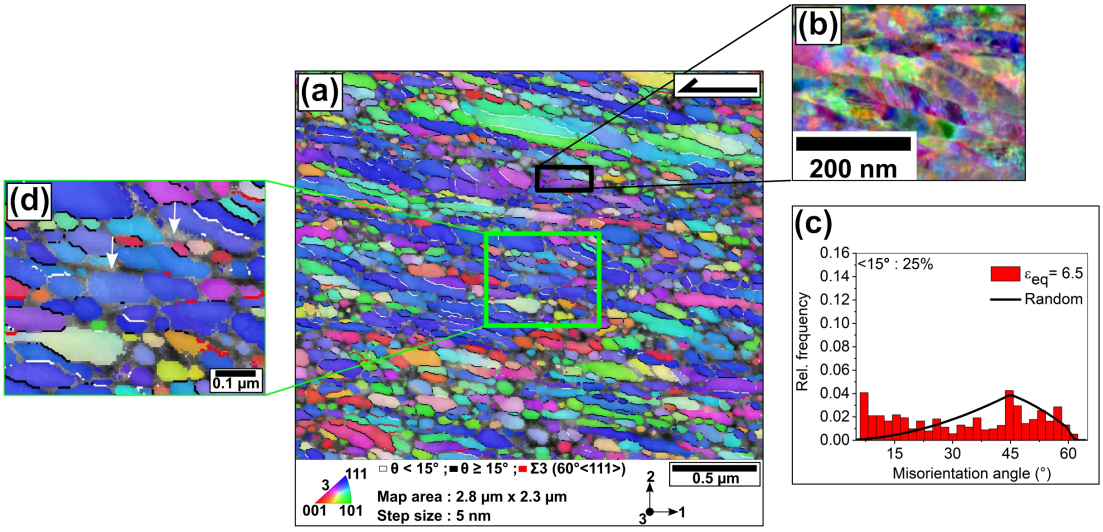

Figure 6: (a) TKD- IPF map of Al_6(CoFeMnNi) after HPCS deformation at ε_{eq}= 6.5, (b) FSD image confirming nano-twins at specific spots (black rectangular box), (c) neighbor-to-neighbor misorientation distribution, and (d) enlarged view of the area inside the green rectangle to point out the presence of grain boundary shearing (examples are indicated by white arrows).

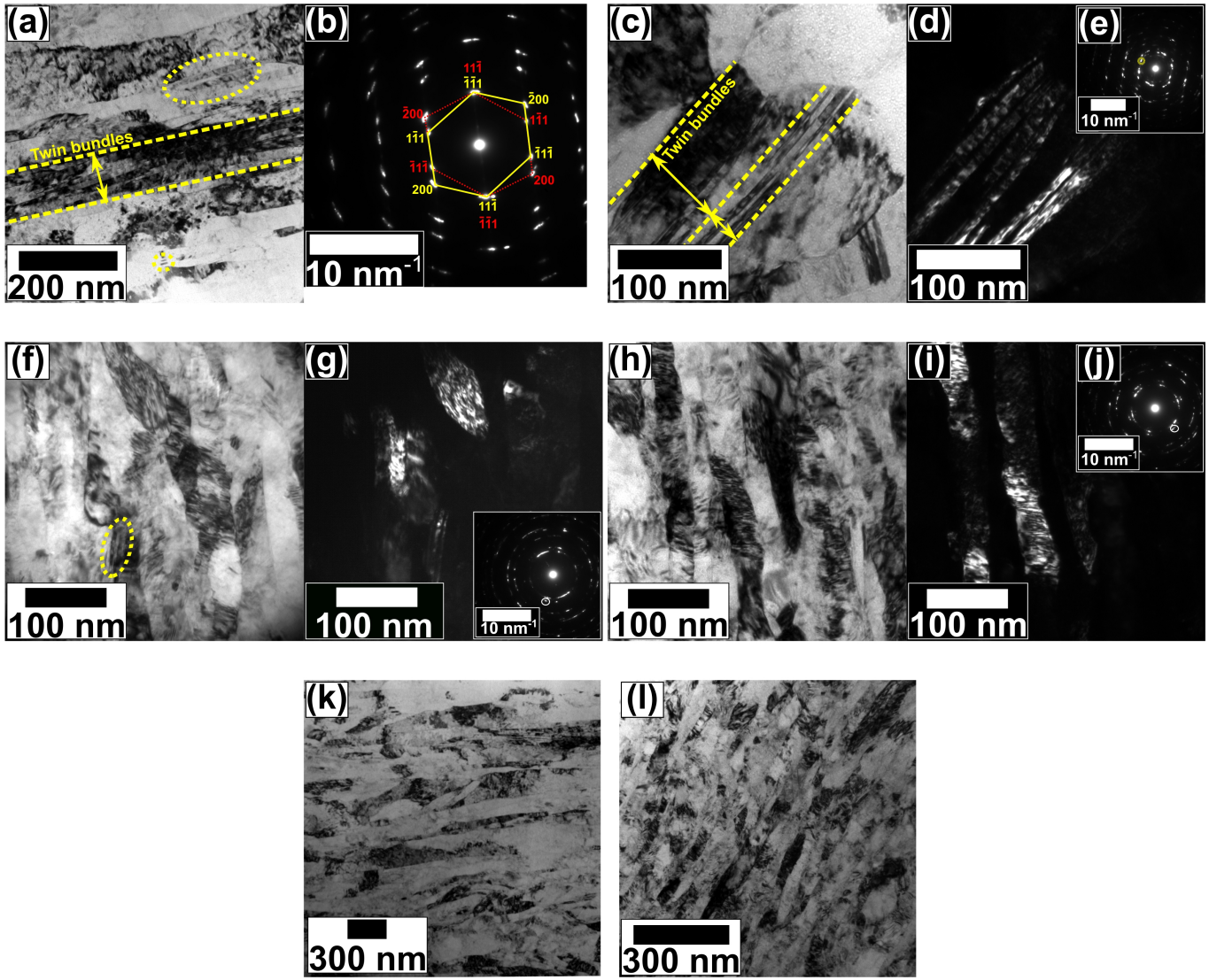

Figure 7: TEM bright field and dark field images along with selected area diffraction patterns with fcc [011] zone axis, (a)-(e)(k) at ε_{eq}= 4.8, and at ε_{eq}= 6.5 (f)-(j)(l).

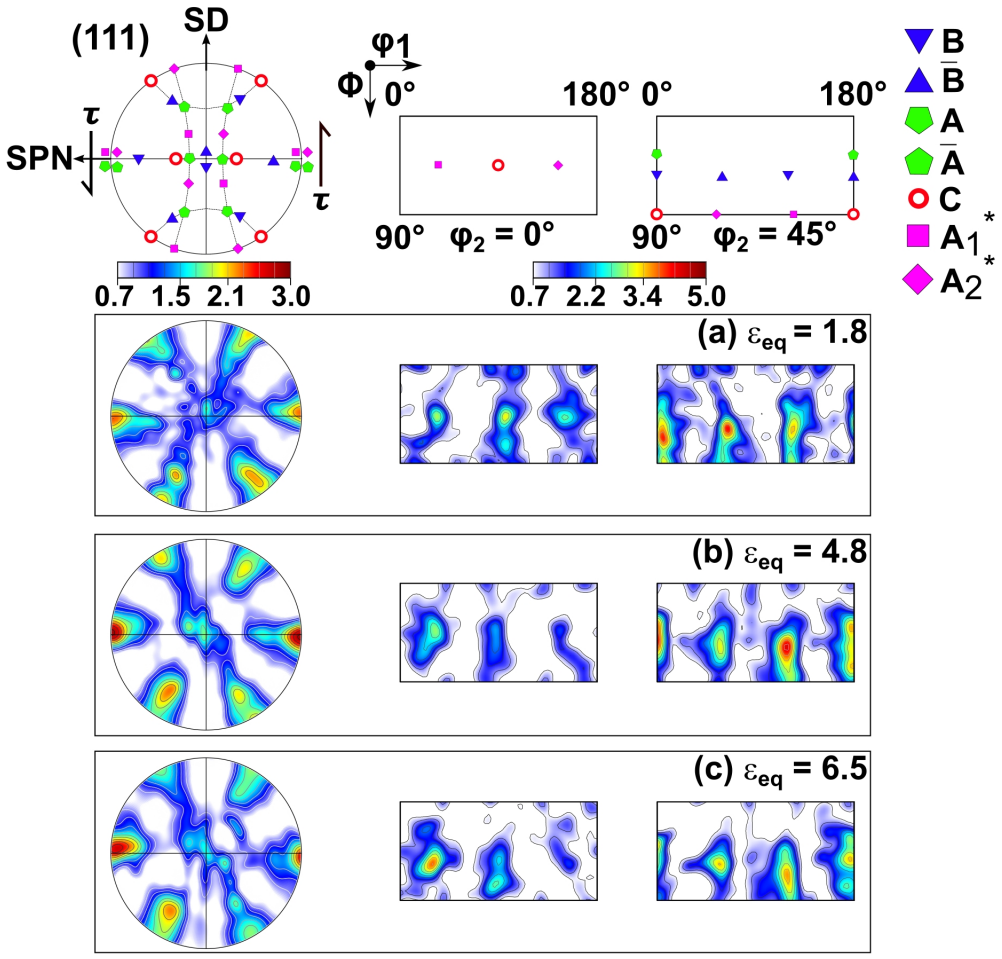

Figure 8: Experimental macro-textures represented in (111) pole figure along with ODFs φ_2 =0° and 45° at different ε_{eq} values. The symbols shown above correspond to the ideal orientations of fcc shear textures.

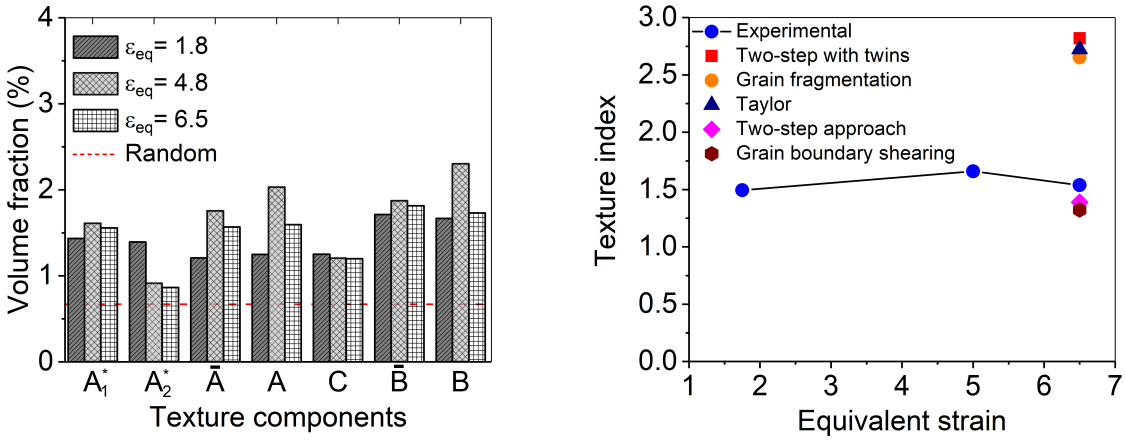

(a) (b)

Figure 9: (a) Volume fraction of the ideal shear components and (b) comparison of experimental and simulation texture index values at different ε_{eq} values.

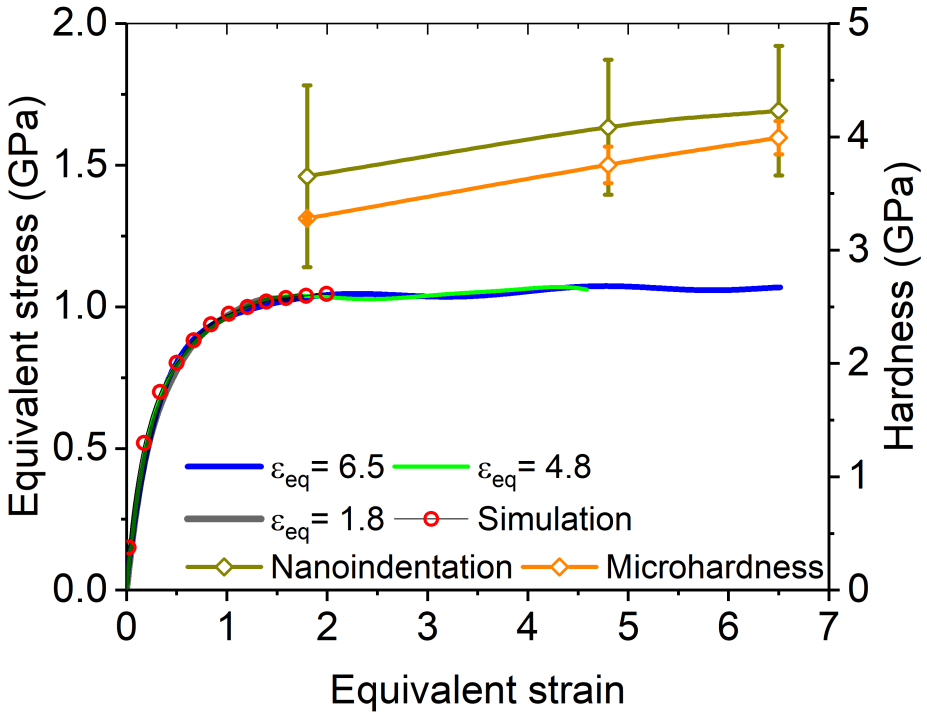

Figure 10: Experimental and simulated strain hardening curves along with nanoindentation and microhardness values as a function of equivalent strain.

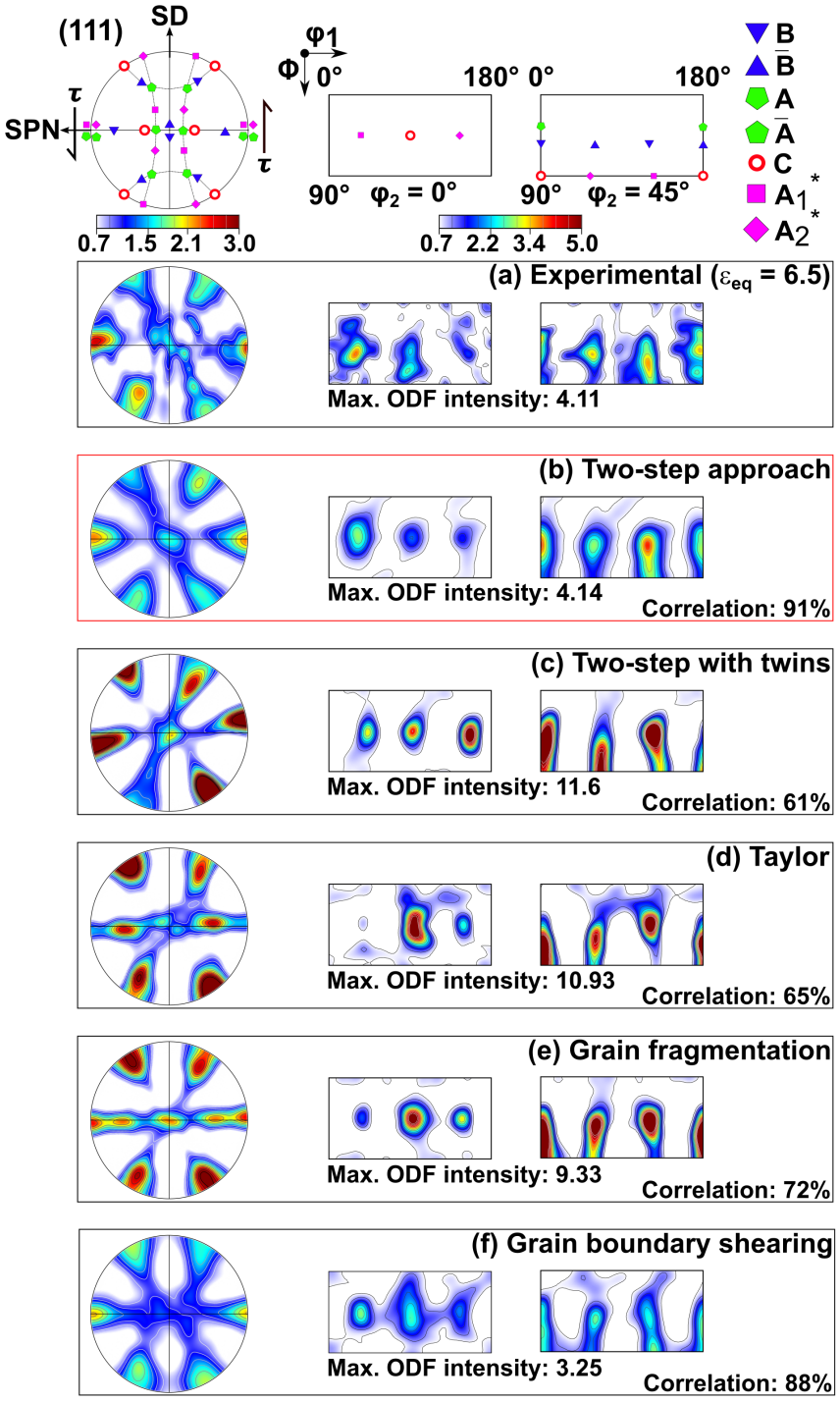

Figure 11: Comparison of experimental and simulated textures using (111) pole figures and ODFs φ_2 = 0°, 45°, (a) experimental texture at ε_{eq}= 6.5, (b), (c), (d), (e), (f), and (g) shows various simulated textures. The symbols shown above correspond to the ideal orientations of fcc shear textures.

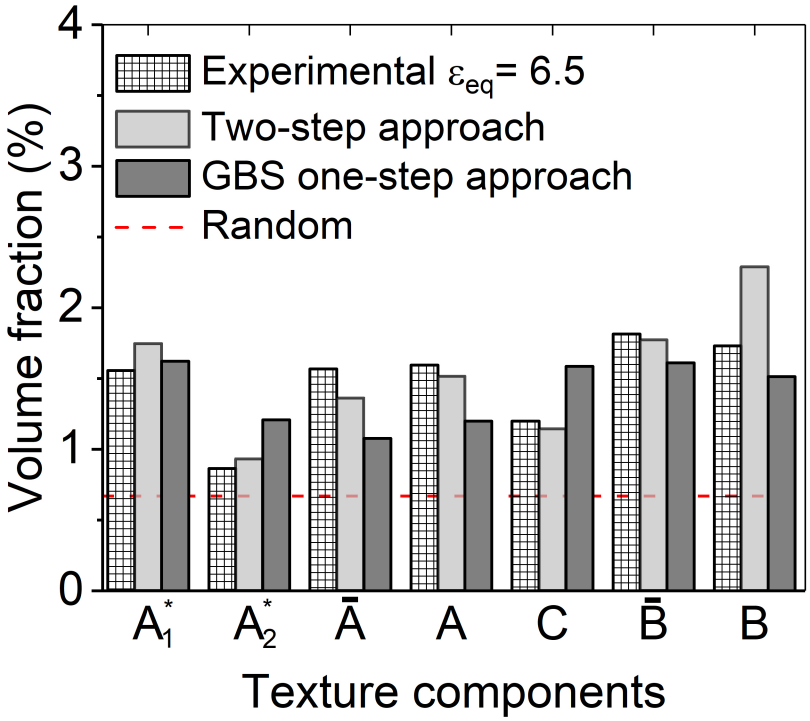

Figure 12: Comparison of volume fractions of the ideal components; experimental and simulated textures.